Physical Conditions in the Ionized Gas of 30 Doradus

R. Indebetouw[1,2], G. E. de Messières[1], S. Madden[3], C. Engelbracht[4], J. D. Smith[4], M. Meixner[5], L. Smith[5,6], B. Brandl[7], F. Boulanger[8], F. Galliano[9], K. Gordon[4], J. L. Hora[10], M. Sewilo[5], A. G. G. M. Tielens[11], M. Werner[12], M. G. Wolfire[13]

remy@virginia.edu, ged3j@virginia.edu

ABSTRACT

We present a mid-infrared spectroscopic data cube of the central part of 30 Doradus, observed with *Spitzer*'s InfraRed Spectrograph. Strong aromatic dust emission features are detected, as well as somewhat weaker emission lines of S II, molecular and atomic hydrogen. The dominant spectral features are emission lines from moderately ionized species of Argon, Neon, and Sulphur, which are used to determine the physical conditions in the ionized gas. The ionized gas excitation shows strong variations on parsec scales, some of which can plausibly be associated with individual hot stars. We fit the ionic line strengths with photoinization and shock models, and find that photoionization dominates in the region. The fitted ionization parameter U traces the rim of the central bubble, as well as highlighting isolated sources of ionization, and at least one quiescent clump. The fitted hardness of the ionizing radiation field T_{rad} reveals several "hot spots" that are either the result of individual very hot stars or trace the propagation of the diffuse ionizing field through the surrounding neutral cloud.

Subject headings:

---

[1]Department of Astronomy, University of Virginia, PO Box 3818, Charlottesville, VA 22903

[2]National Radio Astronomy Observatory, 520 Edgemont Rd, Charlottesville, VA 22903

[3]Service d'Astrophysique CEA, Saclay, 91191 Gif Sur Yvette Cedex, France

[4]Steward Observatory, University of Arizona, 933 North Cherry Ave., Tucson, AZ 85719

[5]Space Telescope Science Institute, 3700 San Martin Way, Baltimore, MD 21218

[6]Department of Physics and Astronomy, University College London, Gower Street, London WC1E 6BT

[7]University of Leiden

[8]Astrophysique de Paris, Institute (IAP), CNRS UPR 341, 98bis, Boulevard Arago, Paris, F-75014, France

[9]NASA Goddard Space Flight Center, Greenbelt, MD 20771

[10]Center for Astrophysics, 60 Garden St., MS 67 , Harvard University, Cambridge, MA 02138

[11]NASA Ames Research Center, SOFIA Office, MS 211-3, Moffet Field, CA 94035

[12]Jet Propulsion Lab, 4800 Oak Grove Dr., MS 264–767, Pasadena, CA 91109

[13]Department of Astronomy, University of Maryland College Park, MD 20742

1. Introduction

The 30 Doradus region of the Large Magellanic Cloud (LMC) is an ideal laboratory in which to study the effect of massive star formation and its feedback on the circumcluster interstellar medium (ISM). Star formation processes in the Magellanic Clouds are potentially a template for the early universe, where small irregular galaxies were commonplace and the overall metalicity lower. In particular, the star formation rate measured relative to molecular mass may be high in the LMC compared to our Galaxy (), but that measurement is complicated by interpretation of CO data in molecular clouds that are known to be more porous and deeply penetrated by ultraviolet radiation, and an uncertain CO-H_2 conversion factor (e.g. Poglitsch et al. 1995; Bernard et al 2008). 30 Doradus itself, the brightest star formation region in the LMC, contains several 10^5 $M_\odot$ of molecular hydrogen traced by ^{12}CO(1-0) (Johansson et al. 1998), much of which is in two elongated clouds that form an arc or ridge in the center of the nebula (see Figure 1). That molecular material is probably only the remnant of the cloud which formed the central cluster and thousands of OB stars. Observations of higher energy CO transitions suggest that this remnant ridge of molecular gas is quite warm and dense (Kim 2007), and near-infrared observations have revealed that it is actively forming new stars (Hyland et al. 1992; Rubio et al. 1998; Maercker & Burton 2005)

The dominant star-forming cluster of the 30 Doradus H II region is NGC7020, whose dense center, R136, is usually considered the nearest super star cluster (SSC). R136a contains 39 O3 stars and a total stellar mass of $\simeq 5 \times 10^4$ $M_\odot$ within 2.5 pc, and stellar densities exceeding 5×10^4 $M_\odot pc^{-3}$ (Hunter 1999; Walborn 1991), clearly remarkable for the local universe. Large extragalactic SSCs are the hosts of one of the most extreme modes of star formation in the universe, may develop into globular clusters, and play a key role in galaxy formation (Johnson 2004). No enormous SSCs such as those found in the Antennae galaxies lie close enough for us to study in refined spatial detail. However, there is a continuum from objects such as Westerlund 1, the largest known star cluster in the Milky Way (Kothes & Dougherty 2007), to the more energetic and massive R136, to the furnaces of the largest extragalactic SSCs containing $\gtrsim 10^6$ $M_\odot$ (Johnson 2004). At a distance of 53 kpc (Brandl 2005), 30 Doradus is close enough to study at the parsec-scale resolution that is required to understand the formation and feedback effects of individual stars, and a prime target for detailed study of the same mechanisms which operate in more distant and massive SSCs.

Observations at mid-infrared (MIR) wavelengths offer several advantages for studying star formation and its interaction with circumcluster dust and gas. MIR (here roughly defined as 5-50μm) continuum emission is dominated by radiation from very small dust grains (VSGs); the broad shape of the continuum is sensitive to the VSG size and temperature distribution, and hence indirectly to the radiation intensity in photon-dominated regions, and to the destruction of smaller grains as would be expected above 2000K and in H II regions. Broad ($\sim$1μm) dust emission features are also prominent between 3 and 19μm. These previously named "unidentified infrared bands" result from distortion (bending, stretching) modes of aromatic molecules containing

tens to hundreds of carbon atoms. (Most features have been attributed to polycyclic aromatic hydrocarbons, PAHs, but unique astrophysical identification is a work in progress). Analysis of relative strengths of PAH features reveals their size and ionization state which is expected to change in intense radiation fields. Scattered starlight can also contribute to the diffuse emission shortward of $\sim$5μm. Extinction by dust in the infrared is low compared to other wavelength regimes. Observations in the MIR can pierce cold molecular clouds and reveal the star-forming regions that they shroud. There are two major bands of absorption by silicate dust at 9.7 and 18μm, whose shape and strength provide further diagnostic of the dust in the region. Mid-infrared (MIR) spectroscopy if the entire 30 Doradus region with *ISO-SWS* (Sturm et al. 2000) revealed a continuum-dominated spectrum with very weak silicate absorption features.

The most recent and sensitive MIR continuum observations of the Magellanic Clouds were obtained as part of the *Spitzer* (Werner et al. 2004) Legacy program "Surveying the Agents of a Galaxy's Evolution" (SAGE), using IRAC (3–8μm Fazio et al. 2004) and MIPS (24-160μm Rieke et al. 2004). The goals of SAGE are to conduct a detailed study of the dust processes in the ISM, to complete a census of newly formed stars in order to find the star formation rate in the LMC, and to study evolved stars with high mass loss rates in order to determine the rate of mass injection into the ISM (Meixner 2006). Figure 1 places the MIR emission from 30 Doradus in its multiwavelength context. 8μm emission traces the same arc-shaped ridge seen in the optical, delineating the edge of a bubble probably blown by R136 and filled with hot X-ray emitting plasma. The remaining molecular material in the region is also located in that ridge. Figure 2 shows the same 8μm image with notable sources labeled.

The MIR contains numerous atomic emission lines from fine-structure transitions that are useful diagnostics for ionic abundances and for the excitation of ionized gas. Also observed are the pure rotational lines of molecular hydrogen, from H_2 S(0) to H_2 S(6), and several of the Humphreys series of atomic hydrogen transitions, from excited states to quantum level 6.

This paper presents a new complete spectral cube of 30 Doradus with the low-resolution modules of *Spitzer*/IRS (Houck et al. 2004). The sensitivity of this dataset vastly exceeds the previous ISOCAM-CVF data (Madden et al. 2006), which only provided maps of the few strongest ionic lines, but tentatively showed a gradient of decreasing excitation in the [Ne III]/[Ne II] ratio as a function of distance from R136, and signs of PAH destruction in the central regions of the nebula. Our dense (spatially contiguous) spectral cube of 30 Doradus allows detailed study of dust and gas properties in an environment that is nearby, bright, and spatially resolved, and which displays many of the IR phenomena which are of great interest in studying SSCs and other sites of extragalactic massive star formation.

The data are described in sections §2. In particular, §2.1 discusses reduction and artifacts, §2.2 the line and feature fitting procedure, and §2.3 quality assurance tests including a comparison with high-resolution IRS data from LeBouteiller et al. (2008). In §3 we describe the general results – the spatial distribution of emission lines and their ratios. §4 describes the derived distribution of

matter – electron density and dust, and §5 the distribution of radiation evident in the excitation of the gas. We confront the data with photoionization and shock models, and summarize and discuss implications in §6.

2. Observations

The *Spitzer* Space Telescope is currently the most capable mid-infrared telescope. Like any satellite infrared observatory, it is free of atmospheric and ground-based thermal contamination. *Spitzer* is $\gtrsim$10 times more sensitive [CHECK!] than the previous premier infrared observatory, *ISO-SWS*, and *Spitzer*'s Infrared Spectrograph IRS has $\gtrsim$10 times higher spatial resolution than the SWS aperture. We used the four low resolution modules of the IRS. The spectral resolution ranges from 60 to 120 (Spitzer Observer's Manual 7.1 2006)[1], with reliable wavelength coverage as described in Table 1. The four modules are the short wavelength / low resolution second order (SL2), short wavelength / low resolution first order (SL1), long wavelength / low resolution second order (LL2), and long wavelength / low resolution first order (LL1). Our data is divided into eighteen Astronomical Observing Requests (AORs) spaced out over our total observation, each containing many records (also called BCDs, or basic calibrated data, in Spitzer Science Center notation), which are pipeline-processed images of the IRS chip.

We observed 30 Doradus over five days in September of 2006, using *Spitzer's* spectral mapping mode in order to obtain detailed spatial information. The total amount of time on target was 74 hours. We used 3440 slit pointings, covering 40.5 square arcminutes in the short-wavelength modules and 69.1 square arcminutes in the long-wavelength modules (see Figure 3). Each slit overlaps half of the preceding one, and each row of slits overlaps half of the preceding row, so every point on the map was observed at four separate slit pointings. There were three repetitions per pointing for the SL observations, at 14 seconds each (for a total time of 168 s for each point on the SL maps), and four repetitions per pointing for the LL observations, at 6 seconds each (for a total time of 96 s for each point on the LL maps). The result is four large and dense spectral cubes, one for each module.

We also made separate observations of a nearby region of comparatively blank sky, bracketing our target observations in time, to comprise background observations and to better characterize rogue pixel response. The total time on background was 44 minutes.

[1]Available at: http://ssc.spitzer.caltech.edu/documents/SOM/

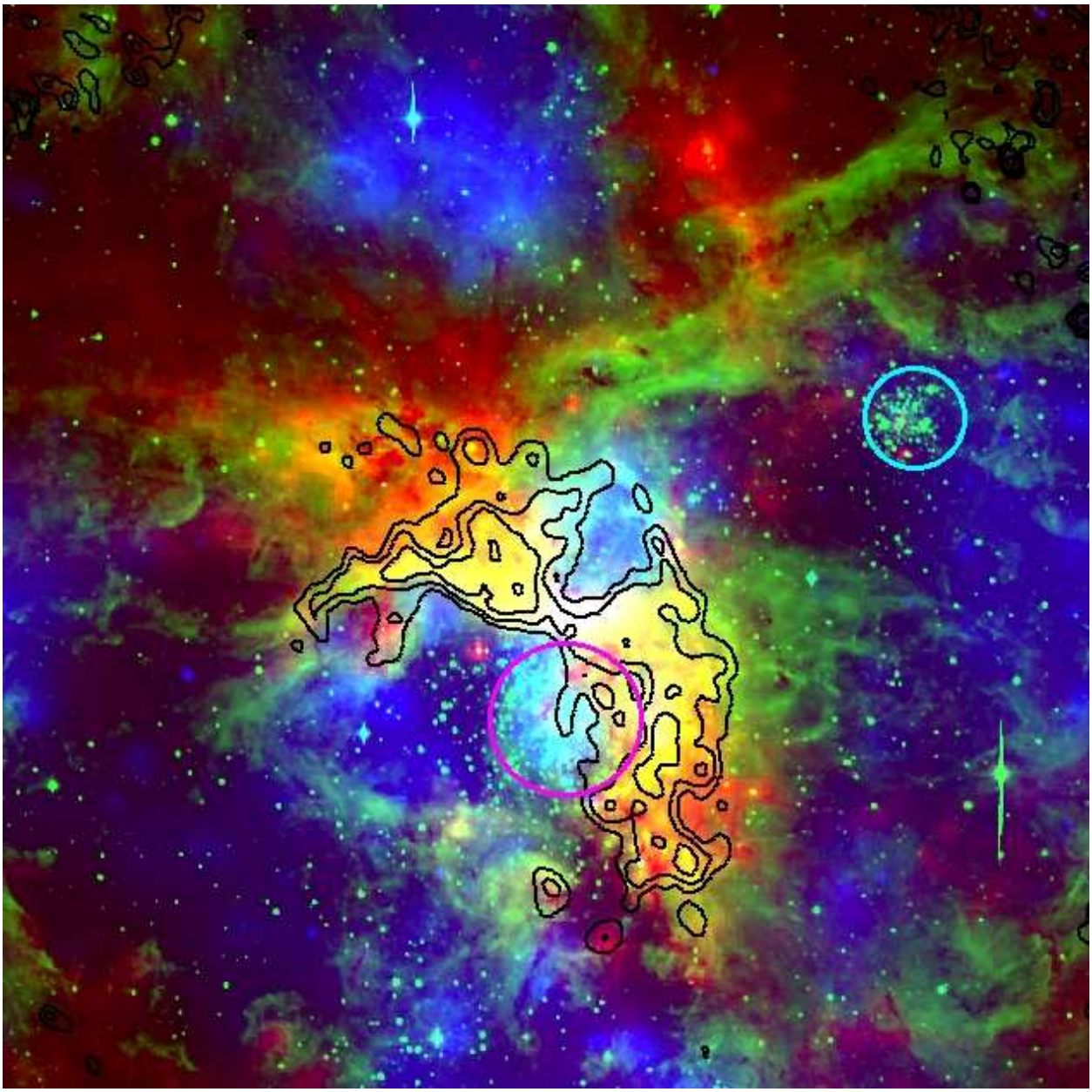

Fig. 1.— The 30 Doradus nebula. Red: IRAC 8μm image. Green: ESO B-band image. Blue: broad-band soft X-ray image, 0.5−2 keV (private correspondence: Leisa Townsley). Black contours: high-resolution 3cm continuum from Lazendic et al. (2003). Magenta mark: the star cluster R136, core of NGC 2070, at $5^h38^m42^s$ -69°06′0″. Cyan mark: the star cluster Hodge 301, at $5^h38^m16^s$ -69°4′0″.

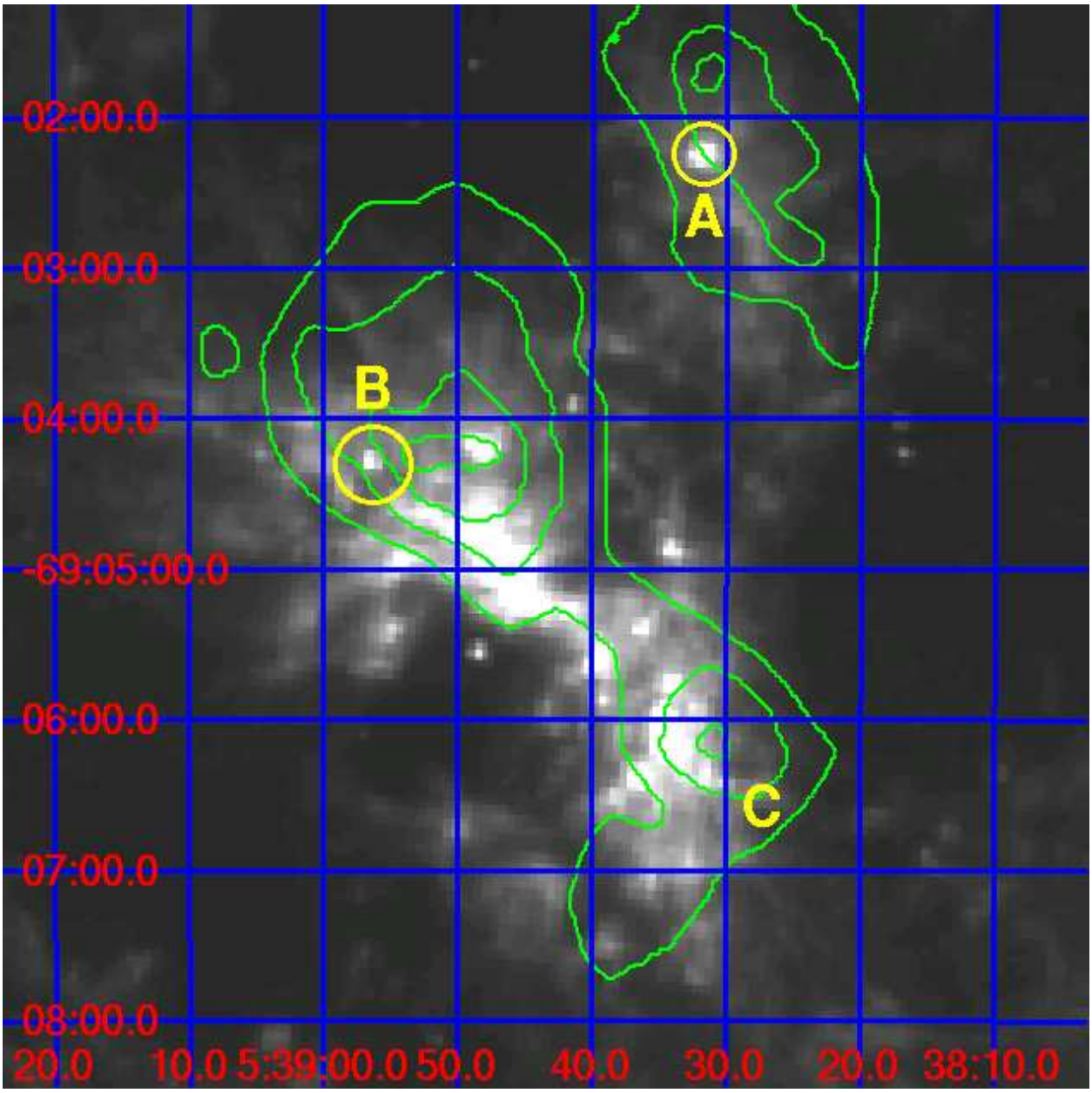

Fig. 2.— IRAC 8μm image with coordinate axes. Green contours: ^{12}CO(1-0) emission (Johansson et al. 1998). The spatial extent of this image is the same as all other maps in this paper, except Figures 3 and 4 [check this]. Some sources of interest: **A:** an IR point source coincident with the molecular cloud [JGB98] Dor-06 (Johansson et al. 1998), at $5^h38^m31.63^s$ -69°02′14.6″. **B:** an unidentified IR point source and location of high excitation. **C:** a region of low excitation associated with the two molecular clouds [JGB98] 30 Dor-12 and 13 (Johansson et al. 1998).

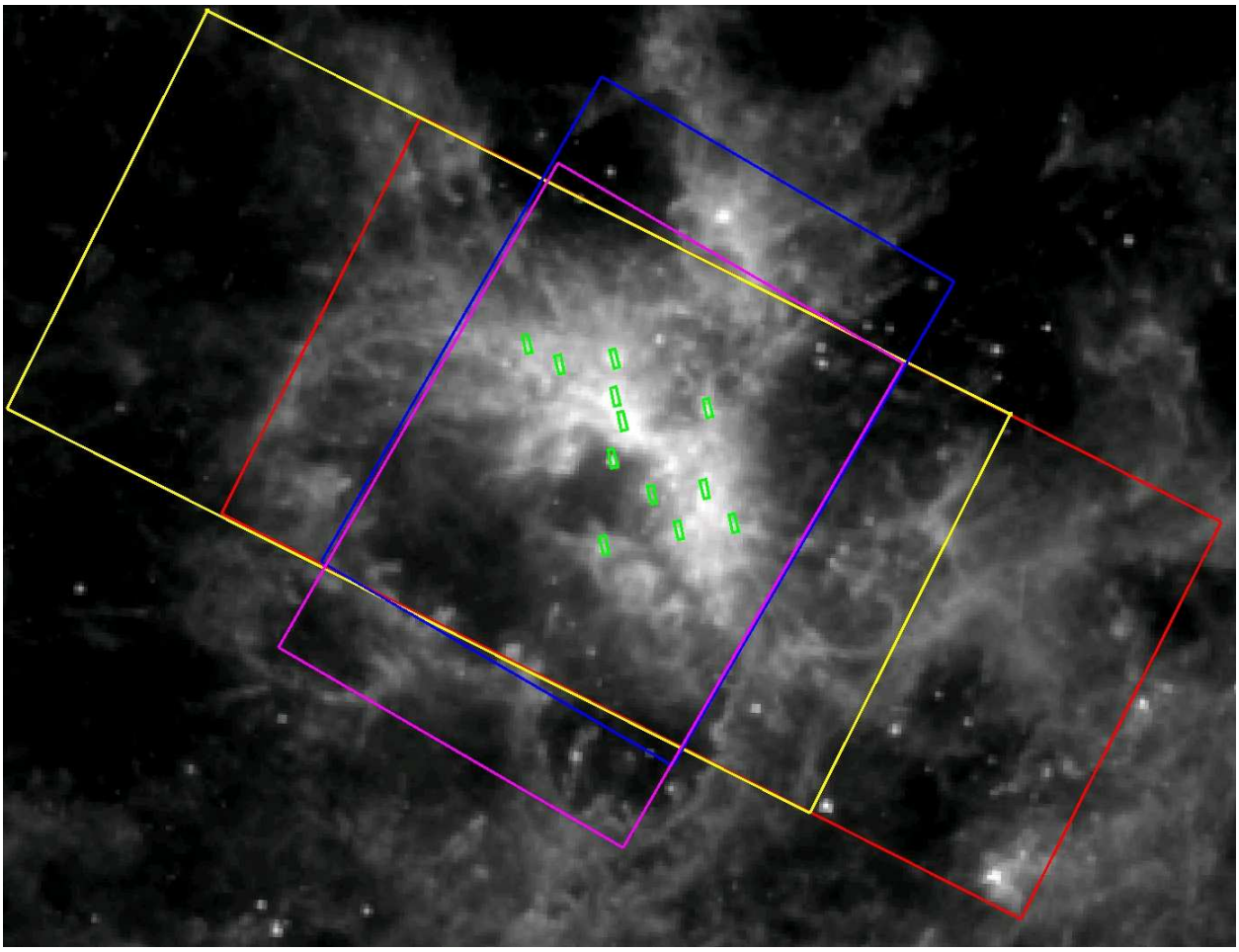

Fig. 3.— IRAC 8μm image with the scope of coverage in each of the IRS modules shown. Red: LL1. Yellow: LL2. Blue: SL1. Magenta: SL2. Green: Brandl's high resolution apertures (see §2.3).

2.1. Reduction of data cube

We used the basic calibrated data from the Spitzer Science Center pipeline version S14.4.0. The main tool for the assembly and reduction of our data cube was CUBISM (Smith 2007b), which is designed for dense spatial IRS maps. The functions of CUBISM include tools to reduce the data (subtracting background, applying a slit loss correction function, trimming the slit in the spatial direction, masking pixels that are flagged by the pipeline, and applying algorithms to identify rogue pixels) and to extract spectra and maps from the data cube.

2.1.1. Background subtraction

Our off-target background observations bracket the data set in time. We chose to take an average (with minima and maxima trimmed) of all the background records and subtract that from all of the data records. It was possible that the two sets of background records could be appreciably different, reflecting a gradual change in the state of the IRS chip [include reference about discussion of this topic?], and that a linear interpolation of the two sets over time would be more appropriate as the background for each data record. Indeed, the mean flux levels of the background records monotonically increases with time [check whether it's truly monotonic, or whether it varies but generally increases], and thus the average of the second set of background records has a slightly higher mean flux level than the average of the first set. We tested three different background subtractions on an aperture from the SL1 module: using only the first set, using only the second, and using the mean of the two sets. There was no appreciable difference in the resulting spectra [quantify this, for small resl extractions], so we concluded that using the mean of all background records is adequate.

2.1.2. Flux calibration

The IRS SL slit is approximately 3.6 arcseconds wide, and the LL is approximately 10.6 arcsecond wide (see Spitzer Observer's Manual 7.1 2006, Table 7.5). Some fraction of the instrument point-spread function (PSF) falls outside of the slit, depending on wavelength. For example, the full width half max (FWHM) of the PSF at 14.5μm, at the upper wavelength range of the SL first order, is about 3.74 arcseconds (see Spitzer Observer's Manual 7.1 2006, §8.1.2.1). The Spitzer Science Center pipeline applies a slit loss correction factor (SLCF) to adjust for this loss of flux for point sources. However, in the case of a spatially uniform extended source, it is more appropriate to use no SLCF, because there is no net loss of flux. CUBISM allows the option of using the SLCF or re-correcting to the original flux levels. In the case of 30 Doradus, an extended source, we opted for the latter. However, it is important to note that in some areas of the map, there are bright features which are neither point sources nor uniformly extended emission, which have some net loss

of flux. The magnitude of this loss is at most 36% (see Sheth 2006, Slide 13)[2] . This loss may be responsible for some of the mismatches we experienced between the fluxes of the four different modules at some points in the map.

2.1.3. Artifacts in data cube

There are three major artifacts which appear in a 2-D map of our data cube at a given wavelength. In all four modules, there are numerous faint stripes, one pixel wide, which cross the map in the direction that the slit scans. In the two SL modules, there is a broad flux discontinuity in one area of the map. The affected region varies with wavelength. There is also a related bright region in the SL modules. The faint stripes appear to be mainly caused by hot pixels on the IRS chip. As the slit was stepped across 30 Doradus, each hot pixel was "dragged" across the map, creating a bright stripe. They can be eliminated via two cleaning methods: wavsamp trimming and rogue pixel masking. The flux discontinuity is caused by saturation in the peak-up image, and must be corrected by fitting a correction factor to the regions of the chip between the SL modules.

The Spitzer Science Center has defined a polygon, called the wavsamp, defining the active area to extract from the IRS chip for each module. In the case of 30 Doradus, the default wavsamp tends to be too generous in the spatial direction, including a few pixels where the spectral response is reduced. By trimming it, we were able to eliminate some of the faint stripe artifacts.

It is possible to determine which pixels on the IRS chip contribute to a given point in the data cube, using a CUBISM tool called backtracking. Backtracking from the artifacts in the maps demonstrated that most, if not all, of the remaining faint stripes are caused by individual rogue pixels, whether hot or cold. In addition to masking the pixels automatically flagged by the Spitzer Science Center pipeline, we employed CUBISM's automatic rogue pixel masking algorithms at both the global and record levels. At the global level, we masked any pixel which deviated by at least 2.5 sigma from the median pixel level in at least 35% of the records. At the record level, it was necessary to be much more conservative to avoid masking out real spectral features. We masked any pixel which deviated by at least 7.5 sigma in 70% of its occurrences in the cube. The procedure missed some pixels which were clearly hot or cold, so we also manually marked a set of global and record level rogue pixels. In the resulting cubes, the faint stripes were greatly reduced.

The other major artifact, the flux discontinuity, is caused by saturated sources on the peak-up image (PUI), primarily by bright point sources in the northern part of the region (see Figures 2 and 4). By examining the records associated with the affected region on the map, we can see that where a source saturates several neighboring pixels in the peak-up image, there is a bleed-over effect that reduces the response of the rest of the IRS chip (BCD image) in those rows, and may increase the response in neighboring rows. The result is broad, uneven dark or bright stripes in a 2D map

[2]Available at: ssc.spitzer.caltech.edu/sust/workshop/2006data2/talks/kartik.pdf

extracted from the cube. The location varies with wavelength because as the PUI is scanned across the bright source in space, the artifact changes position on the BCD frame, i.e. changes wavelength. Simply masking all affected pixels at the record level (removing entire BCDs) results in a hole in the maps at many wavelengths. Instead, we chose to mend the response. We selected all rows that intersected a group of saturated pixels on the peak-up image, with a margin of two rows on either side. These are the affected rows. We found the continuum level in adjacent rows, excluding major emission lines, and linearly interpolated across the affected rows. In the case of affected rows that corresponded to continuum emission, we replaced the values with the interpolated values. In the case of affected rows that corresponded to atomic or PAH emission, we attempted to restore the base continuum level below the emission line by adding the interpolated value, and subtracting out the median value of the affected rows in the region between the SL1 and SL2 chips, which is the bias level of the affected rows. The artifact is reduced, though not eliminated. The result is a complete cube, but with regions that have larger uncertainty (see Figure 4). [can we quanfity the added uncertainty?]

At some wavelengths in the SL cubes, a large region of somewhat elevated emission is still visible after our corrections. This artifact appears to be another result of the saturation in the peak-up images. The response of the chip is elevated for the remainder of the AOR. The appearance of the artifact is most dramatic at the wavelengths of 5.2, 6.3 and 10.7μm, but it is localized in space, and is generally reduced in continuum-subtracted images, because the effect is broad on the BCD frame, so broad but low-level in wavelength as well.

2.1.4. Final adjustments to the spectra

The wavelength range of the spectra needs to be trimmed. The full range of the IRS in each of the four modules includes bins where the response is unreliable. In the LL modules, where the spectrum of 30 Doradus is generally smooth, the drop in response at the red edge of the LL2 module and the increase in noise at the red edge of the LL1 module are evident (see Figure 5). We trimmed the LL modules based on these observations. The spectrum of 30 Doradus is more complex in the SL modules, however, with many emission lines and an unclear continuum. In order to determine the range of wavelengths which can be trusted in each SL module, we used the IRS low resolution staring mode spectrum of α Lacertae, an A1 dwarf star whose smooth spectrum is well known. As seen in Figure 5, in each of the SL modules, the spectrum departs from its flat curve at the margins. We trimmed our SL spectra to the wavelengths where the IRS spectrum of α Lac stayed faithful to the flat curve. We also found, based on some spectra from 30 Doradus, that the limit at the red edge of the SL1 module based on the spectrum of α Lac was not conservative enough; consequently, we decreased the trusted upper limit on wavelength for the SL1. We could not use the spectrum of α Lac to determine the reliable wavelengths for the LL modules because the stellar spectrum has low signal-to-noise at such red wavelengths. See Table 1 for our results.

After extracting our spectra, we found that some of the SL spectra were suspiciously low, even

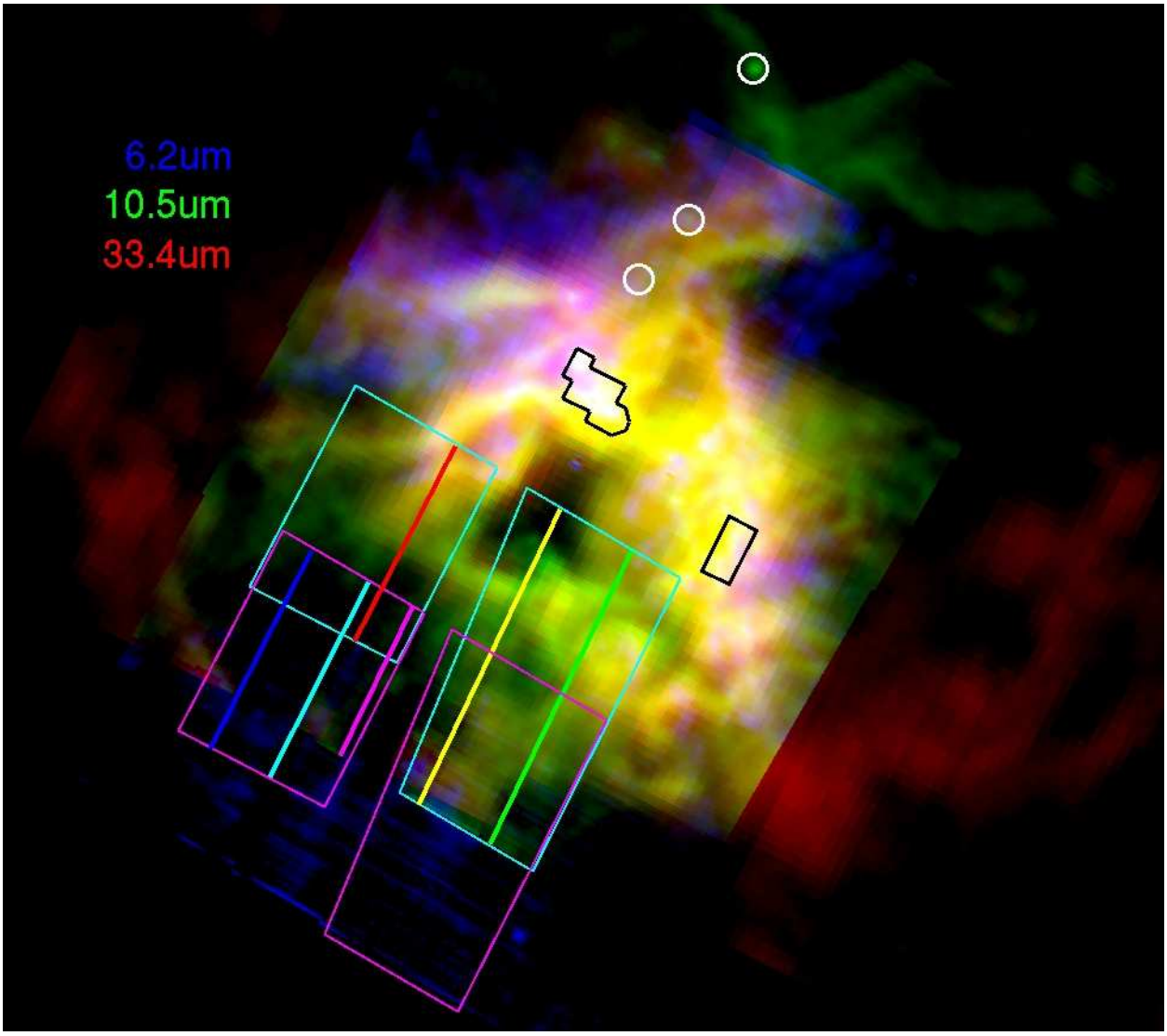

Fig. 4.— Three-color log-scale IRS image with regions of interest overlaid. The emission line maps are continuum-subtracted, and each is plotted at a scale that brings out detail. Red: [S III]λ33.4μm, in the LL1 module. Green: [S IV]λ10.5μm, in the SL1 module. Blue: PAH at 6.2μm, in the SL2 module. The areas outlined in black are vulnerable to falling response or saturation in the LL1 module. Continuum fits in these areas should be regarded with caution, as should the fitted line strengths of long-wavelength emission lines. The sources marked in white saturated the peak-up camera and caused dark stripes and other artifacts in the SL modules elsewhere in the map. The cyan regions represent the total affected area for the SL1 module, while the magenta regions represent the total affected area for the SL2 module. However, the main effect of the saturation is a stripe across the uncorrected map that changes with wavelength, and there are generally no severe effects in the rest of the region for a given wavelength. The approximate location of this stripe is marked by a series of bold lines, for several wavelengths corresponding to major emission lines in our spectra. Blue: [Ar II]λ7.0μm. Cyan: PAH at 6.2μm. Magenta: Humphreys-γ λ5.90μm. Green: [Ar III]λ9.0μm. Yellow: [S IV]λ10.5μm. Red: [Ne II]λ12.8μm. See §2.1.3 for more detailed discussion.

Table 1: Reliable wavelengths

IRS module	Blue limit (μm)	Red limit (μm)
SL2	5.2	7.6
SL1	7.5	14.2
LL2	14.3	20.6
LL1	20.5	35.5

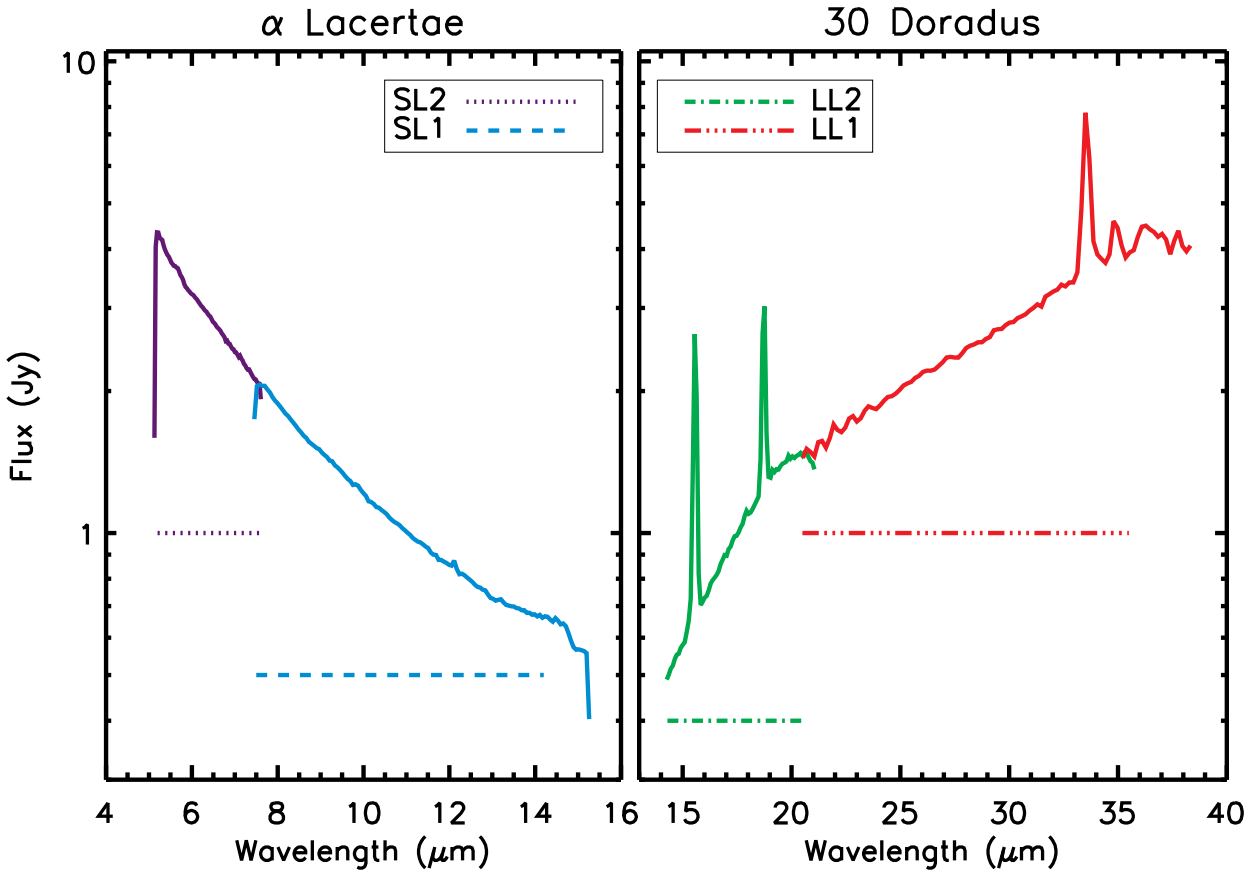

Fig. 5.— Left: The SL spectrum of α Lacertae. Right: the LL spectrum of the R136 region of 30 Doradus. The limits of sensitivity of each module are evident where the smooth continuum level drops off or becomes noisy. Our chosen range of trusted wavelengths for each module is shown with a horizontal bar (see Table 1).

negative for some counts. This may be a problem with background subtraction, and thus requires an additive correction. We raised both SL modules by the additive quantity necessary to make the floor of the SL2 spectrum non-negative.

The different modules of an IRS spectrum do not always match up well in flux. The mismatches between the SL1 and SL2 modules, and the LL1 and LL2 modules, were rarely serious. However, we noticed more consistent mismatches between the SL1 and LL2 modules. The primary cause is probably that the emission in the 30 Doradus region is often best characterized as neither a point source nor as a uniform extended source, but instead as something in between. We have treated it as a uniform extended source (see §2.1.2). Therefore, there is undoubtedly some flux lost. This would call for a multiplicative correction. We found logarithmic fits to the continuum emission in each module close to the junction and multiplied the SL spectra by the ratio of the fits in the overlapping wavelengths.

30 Doradus has a positive velocity of 274 km/s (Feast 1960). The resulting redshift, $z = 0.000914$, is too small to justify redshift-correcting the spectra.

2.2. Spectral Features and Line Fitting

The MIR spectrum of 30 Doradus displays prominent dust features (see Figure 6). Emission from small grains is responsible for the overall shape of the continuum and its strong rise toward the red starting at about 9μm [check the value of the turnover]. Stellar light also contributes to the continuum, particularly toward the blue end of the MIR band, but in 30 Doradus, the emission from dust dominates. Using the fitting package PAHFIT (Smith 2007a), we fit the continuum with an assortment of four thermal functions from 40 to 300K and a stellar blackbody peaking at 5000K.

The broad PAH bands and unresolved atomic lines are blended in some parts of the spectrum. In order to decompose them, we fit the whole suite of emission lines at once. Detailed analysis of the dust features will be addressed in a future work. The feature of greatest potential contern is blending of [Ne II]λ12.8μm with the 12.7μm PAH feature. The PAH contribution is much lower than the atomic line over much of 30 Doradus. In particular, Sturm et al. (2000) found that at the higher resolution of *ISO-SWS*, the ratio of the 12.7μm PAH feature to [Ne II]λ12.8μm was 0.0 within the two *ISO-SWS* apertures (located on the ridge as marked in Figure [X]) – the lowest of any H II region they studied. We used comparisons with high-resolution spectra (see more discussion below) and tests in parts of 30 Doradus that should be completely PAH-free, like the core of R136, to determine that the joint fitting of those two features is robust in 30 Doradus and uncertainties are properly acocunted for.

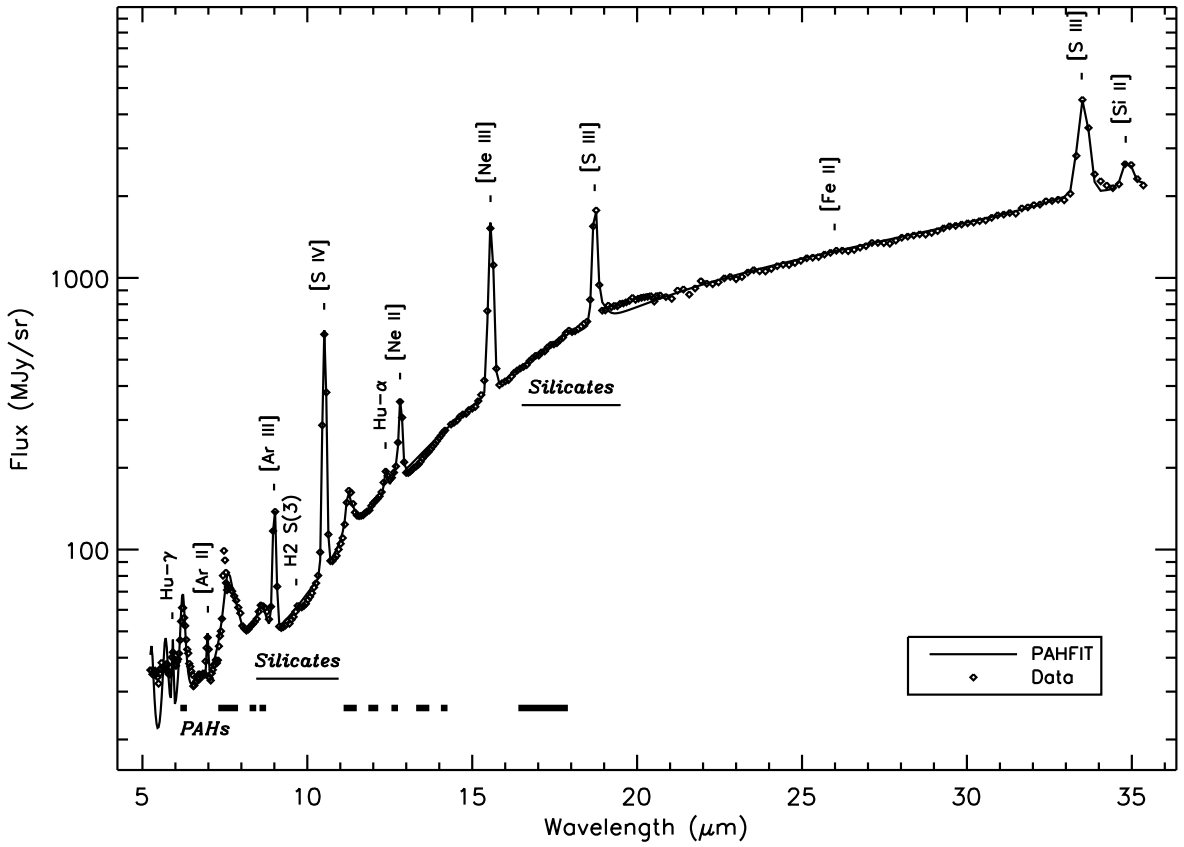

Fig. 6.— A typical IRS spectrum from a relatively faint part of 30 Doradus. The observed spectrum is plotted with symbols, while the fit we made is displayed with a solid line.

2.3. Quality Assurance

In order to check our work on reducing the spectral map, we compared our spectra, taken with the low resolution modules of the IRS in mapping mode, to spectra of several areas of the 30 Doradus nebula taken by Bernhard Brandl with both the low and high resolution modules of the IRS, in staring mode (private correspondence, [add Vianney citation in text and brandl AOR numbers in a footnote]). Brandl's apertures are displayed in green in Figure 3. By selecting the subsets of our map that coincide with Brandl's apertures, we can produce spectra which should be consistent with his. We applied PAHFIT, the same fitting algorithm that we use on our spectral map, to Brandl's spectra. We made some adjustments to PAHFIT to allow for the much higher spectral resolution in his spectrum redward of about 10μm, where there is coverage from the high resolution modules.

In Figure 7, the fitted spectra from two of these apertures are shown. The overall agreement in the shape of the spectrum is clear, with a notable exception in the continuum from 20 to 32μm. The cause is partial saturation in the LL1 module. The high resolution modules are less vulnerable to saturation at these wavelengths. In the upper panel, taken from an aperture toward the south of the 30 Doradus nebula where the continuum emission at long wavelengths is relatively faint, the agreement between our spectrum and Brandl's is close, but the effect starts to become noticeable. In the lower panel, taken from a brighter part of the 30 Doradus nebula where the falling response in the LL1 is more severe, the difference between the low and high resolution spectra is larger. In the brightest parts of the nebula, the LL1 completely saturates. Aside from this predictable effect, the agreement in overall continuum shape between Brandl's spectra and ours is close.

We are most concerned with whether we can obtain the same emission line strengths by fitting Brandl's spectra in the same manner as ours. Figures 7 and 8 show that the PAHs have similar profiles, while the unresolved atomic lines are narrower with higher central intensities in the high resolution spectra. The integrated strengths of several of the emission lines of interest are plotted in Figure 9, for twelve of Brandl's spectra and the apertures from our map that coincide with his. Perfect agreement falls along the line of unity.

The fits to the PAH complex at 11.3μm agree well only at low strength. This may be because of detailed fine structure that appears in the PAH complex at high resolution. In the low resolution spectrum, only a broad feature at 11.3μm, with a shoulder at 11.0μm, is apparent. A Drude profile is sufficient to fit that, and a more complex fitting profile would not be appropriate because of the lack of resolution. In the high resolution spectrum, the shoulder at 11.0μm resolves into a completely separate PAH (see Figure 8), and the main PAH feature at 11.3μm assumes a different profile that would require a more complex fitting algorithm. Thus, we are not concerned about this disparity. The conclusion is that PAHFIT is adequate for fitting PAHs at low resolution, but may not sufficiently describe the same features at high resolution– not surprising, as the list of features used in PAHFIT was empirically tuned using low resolution spectra.

A systematic disparity is evident in the comparison of the Humphreys-α λ12.37μm fitted line

strength. Upon closer examination, two factors surfaced. Both support the trend that the fitted line strength at low resolution is higher than the line strength at high resolution. First, the fainter molecular hydrogen line, H_2 S(2) $\lambda 12.28\mu$m, is resolved in high resolution. The fit to the high resolution Humphreys-α line therefore does not include any of the flux from the molecular hydrogen line. Meanwhile, in the low resolution spectrum, the flux from both lines contributes to the same broad feature. We are confident that Humphreys-α contributes most of the flux we see in low resolution, in part because the line center more closely coincides with 12.37 than with 12.28μm, and in part because, as we can see in the high resolution spectra, the Humphreys-α line is equal to or stronger than H_2 S(2) in all of the areas of our map covered by Brandl's high resolution spectra. However, the flux of both emission lines is contributing to the fit, and so to some extent, our fits to the line strength of the Humphreys-α line are overestimated. This effect is weakest in the parts of 30 Doradus dominated by ionized gas that are the focus of this paper, but should be kept in mind for analysis of the outer parts of the region and PDR physics in future papers. The second factor that contributes to the disparity seen in the second panel of Figure 9 is the PAH feature at 12.6μm. As discussed above in the context of the PAH complex at 11.3μm, the fitting package PAHFIT is intended for the relatively smooth features seen in low resolution, and does not handle the complex morphology of PAHs seen at high resolution as well. In the case of the PAH at 12.6μm, its line strength in the high resolution fit is generally overestimated. Its broad wings thus lead the strength of the Humphreys-α line to be underestimated in the high resolution fit. The slight overestimation of the line in the low resolution spectrum and the slight underestimation of the line in the high resolution spectrum both contribute to the disparity.

The results for the forbidden neon lines, as for most of the stronger lines, show a tighter correlation. The close agreement in the fits to the low and high resolution spectra for the weaker [Ne II]$\lambda 12.8\mu$m is particularly encouraging because one of our concerns in interpreting the neon ratio was the possible entanglement of the [Ne II] atomic emission line with the above-mentioned PAH at 12.6μm. In the high resolution spectrum, the PAH (with its often-unusual shape) and the atomic line are resolved. As in the case of the Humphreys-α line, the strength of the [Ne II] line may be slightly underestimated because of the poor, overestimated fit to the PAH at 12.6μm. The close agreement between the low resolution and high resolution fit, across almost all of the twelve apertures, regardless of PAH strength in each aperture, indicates that there are no systematic errors to the low resolution fit that do not also appear in the high resolution fit. Thus, our results may share the slight bias toward underestimating the [Ne II] strength, but we are generally able to decompose [Ne II] and the PAH at 12.6μm despite the lack of spectral resolution.

Finally, the correlation for the fitted line strength of [Ne III]$\lambda 15.5\mu$m is similarly good, with the exception of two apertures where the high resolution fitted line strength is significantly higher than the low resolution fitted line strength. These two apertures exemplify the extreme of the trend shown in Figure 7, where the response in the LL1 module falls until the module finally saturates. In these cases, our fit to the continuum with thermal dust components is not very successful. The fitted continuum is dragged down in the area from 20 to 32μm, which forces it up in the region of

15μm. This causes our estimation of the strength of [Ne III] to be underestimated.

For these two anomalous apertures, we conducted a test by removing the faulty LL1 spectrum and fitting only the remaining spectrum, to get a better estimation of continuum in the region of [Ne III]. This increased the fitted strength of [Ne III], though not enough to get it to agree with the value we obtained by fitting the high-resolution spectrum.

[Do we want to talk about MIPS/SED reduction here? We don't really use those maps for this analysis, but it should go in a PDR paper, or on its own as a letter?]

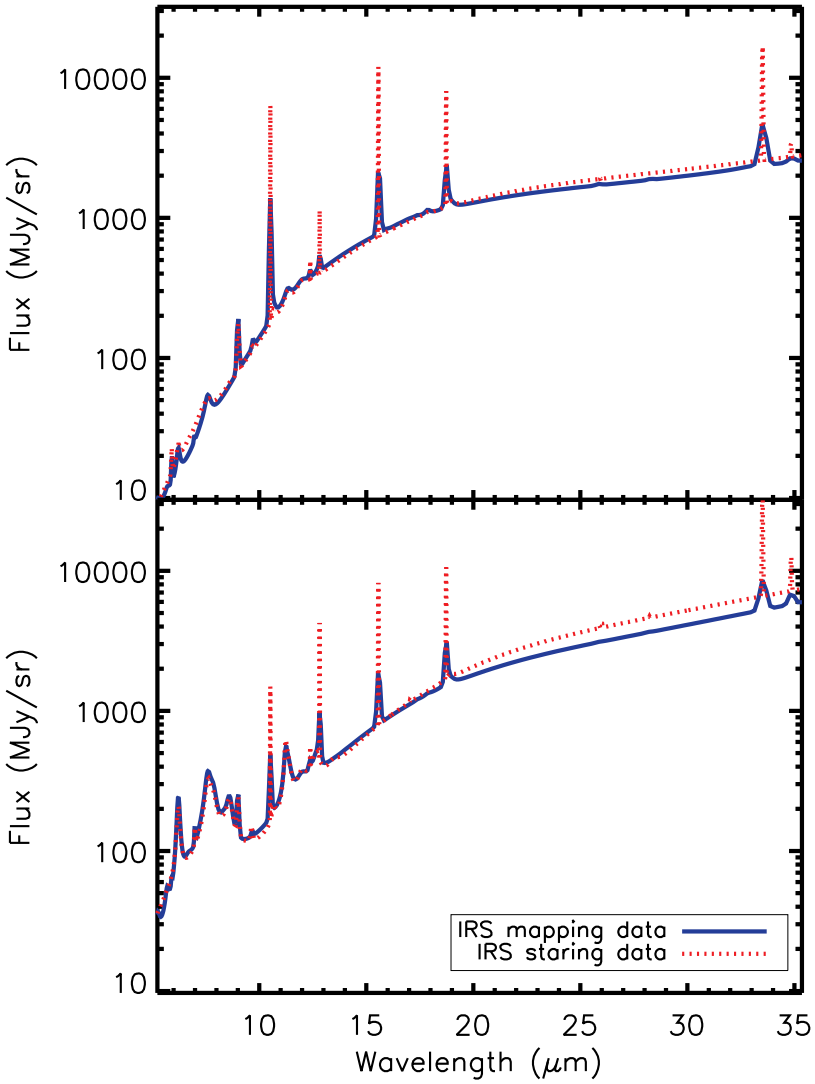

Fig. 7.— In blue, the fit to our low resolution mapping-mode spectra. In red, the same type of fit applied to Brandl's staring-mode spectra, with high resolution data at long wavelengths combined with low resolution data at short wavelengths (the transition is at about 10μm). Top: a relatively faint area in the southern part of the 30 Doradus nebula. Bottom: a brighter area, where the low resolution spectrum suffers from partial saturation and falling response in the LL1 module.

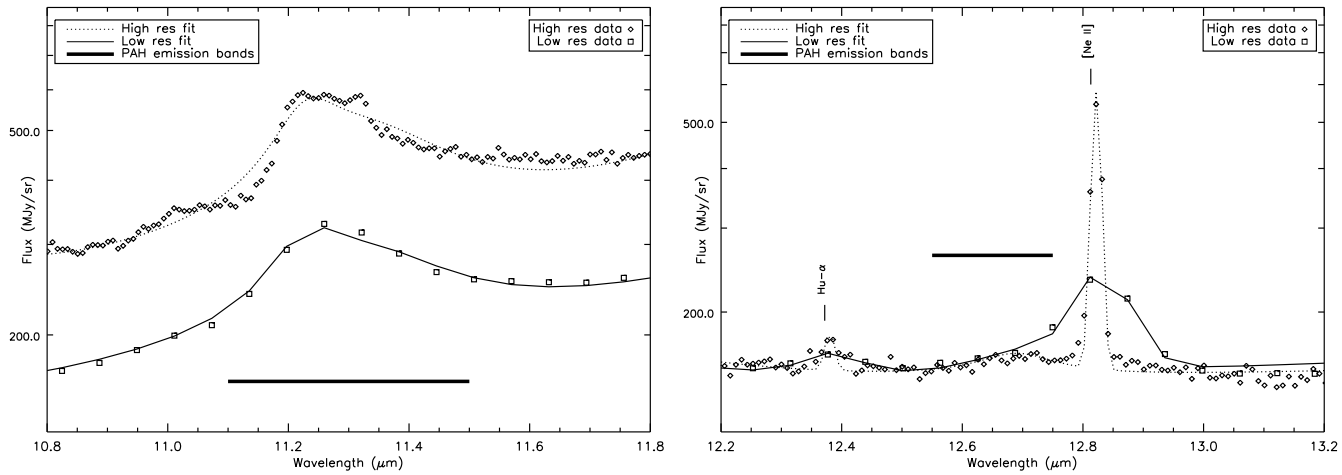

Fig. 8.— Two comparisons of our low-resolution IRS data to Brandl's high-resolution IRS data for narrow wavelength regions. (The two panels are drawn from different regions on the sky, but for each panel the high and low resolution spectra are both extracted from the same aperture on the sky.) Both the measured spectra (symbols) and our fits made with PAHFIT (solid and dotted lines) are displayed. Note that while Brandl's spectrum has higher resolution for the lines, and the continuum strength may vary, the overall strength of the lines agree. Also note that the PAH has a fairly smooth appearance in the low-resolution plot and a more complex morphology in the high-resolution spectrum, which can cause problems when attempting to fit PAH strength in high-resolution. See §2.3.

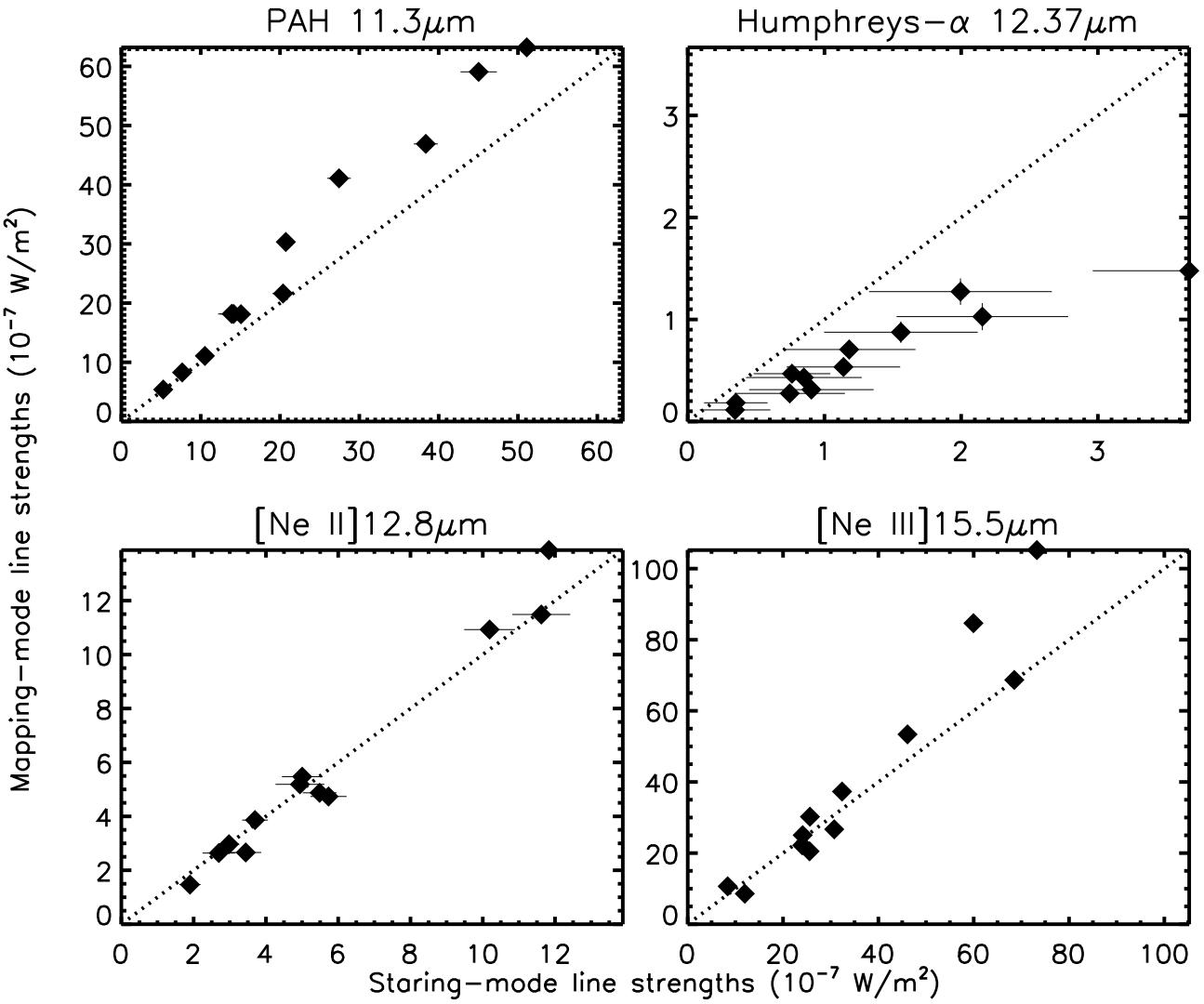

Fig. 9.— Comparison of the fitted integrated strengths of four emission lines. On the horizontal axis are the results from our mapping-mode spectra. On the vertical axis are the results of using the same type of fit on Brandl's high resolution staring-mode spectra. Each symbol represents one area of the 30 Doradus nebula, with horizontal and vertical error bars. The discrepancies from the line of unity are discussed in §2.3. Among those discrepancies, the fitting algorithm we used is not designed to fit the more complex structure of PAHs that resolves in the high resolution spectrum. One reason for the discrepancy in the Humphreys-α is that our fits to the line also include the fainter H_2 S(2) λ12.28μm emission line, which is not resolved at low resolution.

3. Results

3.1. Spatial distribution of emission

Figures 10-12 show maps of ionic line emission in 30 Doradus. To first order, line emission follow the diffuse emission pattern seen at other wavelengths, of a broad arc or "ridge" surrounding an evacuated hole (see Fig 2 for annotations). The overall excitation of the region is immediately clear from the distribution of [Ar II] and [Ar III]– there is no detected [Ar II] in the evacuated hole. With an ionization potential of 15.7eV, charge transfer with hydrogen ensures very little Ar^{+} within an H II region. [ref for charge transfer] We note that the Ar^{++} recombination rate is highly uncertain, so absolute calibration of [Ar III]/[Ar II] has large systematic uncertainty (Morisset et al. 2004; Stasińska & Schaerer 1997). The similarity of overall morphology amongst the Ar, Ne, and S lines suggests that any variation of excitation across the nebula will be correlated with the structure seen in continuum from radio to infrared, although as we will explore thoroughly below, the shape of the hole varies somewhat, and there are some distinct locations of high excitation. The [Si II] distribution appears somewhat displaced away from R136 and the cavity, as would be expected since the line is strong in PDRs as well as ionized gas.

There is a peak in both Ar lines at $5^h38^m28^s$ -69°06′30″, just to the west of the main ridge. The location, marked C on Figure 2, was noted as an IR source (#29) by Hyland et al. (1992), and is a low point in the excitation ratios [Ar III]/[Ar II], [Ne III]/[Ne II] and [S IV]/[S III]. The spectrum if this region is shown in Figure 13.

Lower ionization species have tentative detections in a few places, but never very strongly or widely distributed. Of particular interest is a peak near $5^h38^m44.9^s$ -69°05′13″, at which we detect [N III]λ57.3μm, [O I]λ63.1μm, and [Fe II]λ26.0μm (see the northeastern region marked in Figure 12). This region is affected somewhat by saturation in the LL1 module (>20μm), so we consider the [Fe II]λ26.0μm detection tentative. The ratios of [Ne III]/[Ne II] and [S IV]/[S III] (and the MIR continuum) are high in this general area, but this region in the center of the ridge is complex, and the higher ionization species do not peak in exactly the same location as these lower ionization species. In fact, the peak of low-ionization species falls between two peaks of the [Ne III]/[Ne II] map.

Higher excitation species [O IV] and [Ne V], which have strong lines in the IRS bandpass, are not detected in our maps. As discussed in §5.2, this favors photoionization over shocks as the dominant physical process in the region.

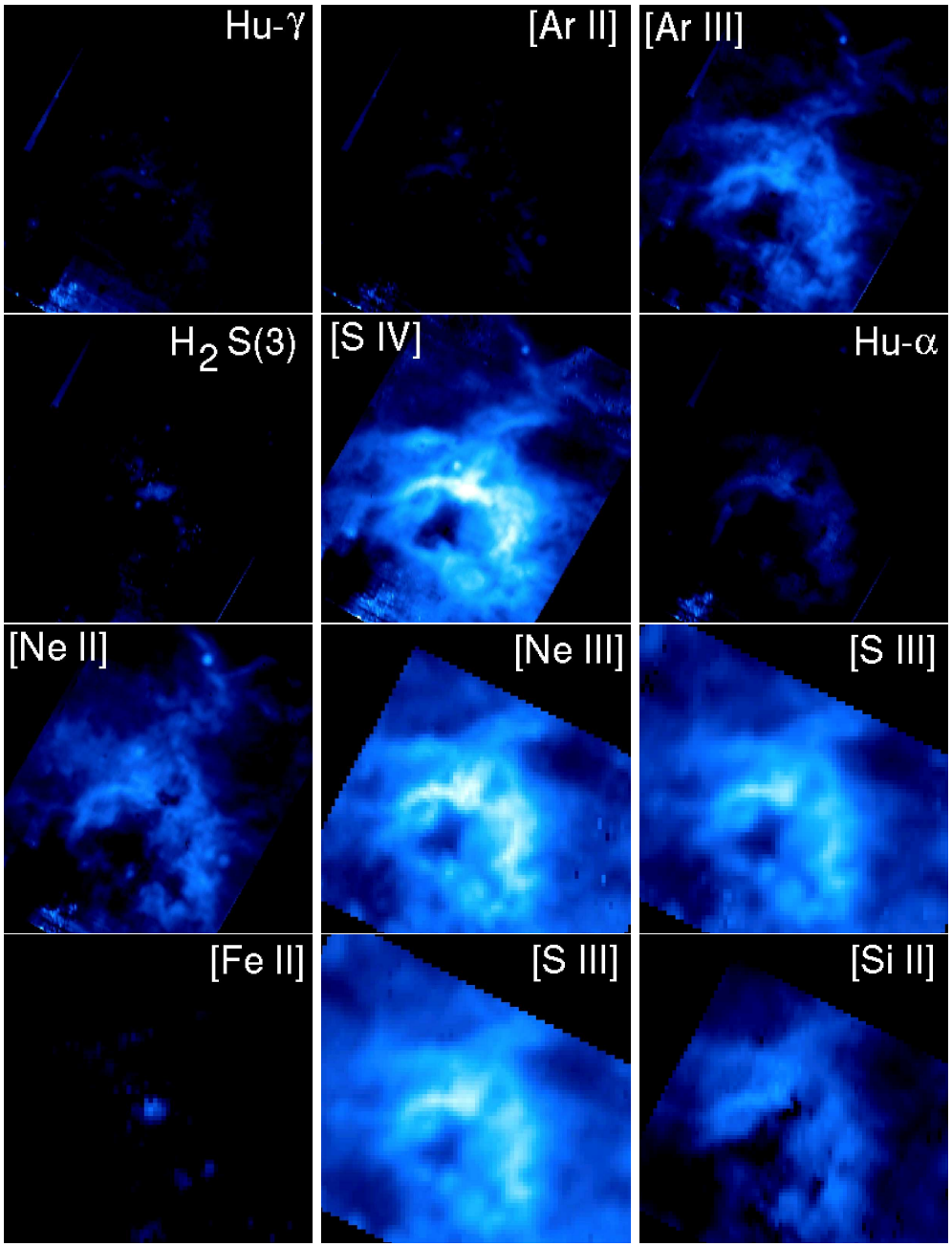

Fig. 10.— Fitted atomic line maps. In order: Humphreys-γ λ5.90μm, [Ar II]λ7.0μm, [Ar III]λ9.0μm, H_2 S(3) λ9.67μm, [S IV]λ10.5μm, Humphreys-α λ12.37μm, [Ne II]λ12.8μm, [Ne III]λ15.5μm, [S III]λ18.7μm, [Fe II]λ26.0μm, [S III]λ33.4μm, [Si II]λ34.8μm. All plots are on the same log brightness scale and the same color contrast scale, and all cover the same region of the sky. For a coordinate grid, see Figure 2.[These figures, and those in the next two figures, are a little more zoomed in than in the B&W overview. They will be fixed later.]

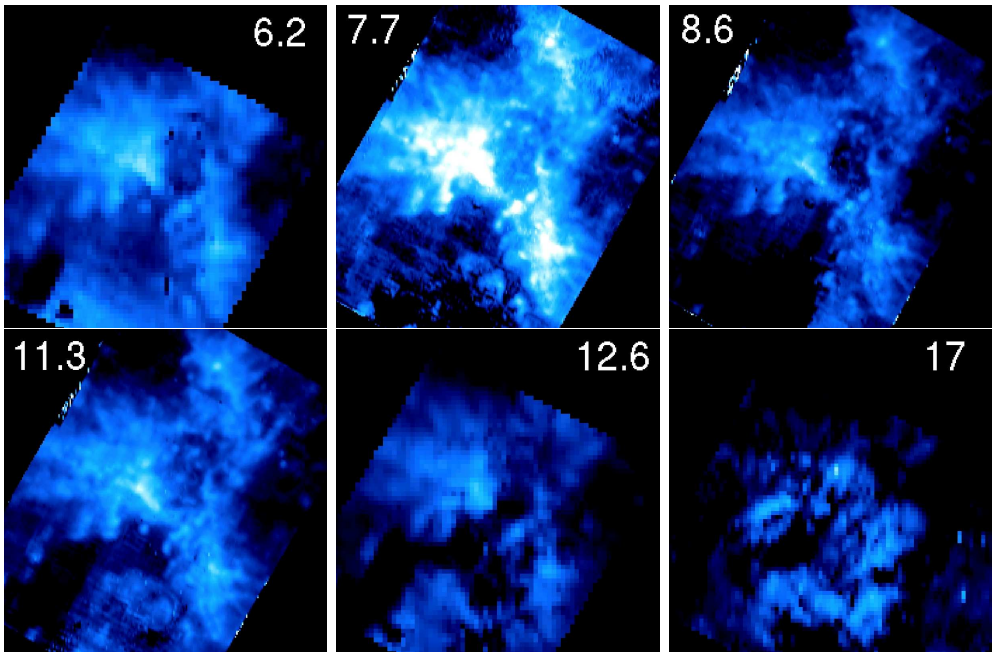

Fig. 11.— Fitted PAH line maps. In order: PAH 6.2μm, PAH complex 7.7μm, PAH 8.6μm, PAH complex 11.3μm, PAH complex 12.6μm, PAH complex 17μm. All plots are on the same log brightness scale and the same color contrast scale as the plots in Figure 10.

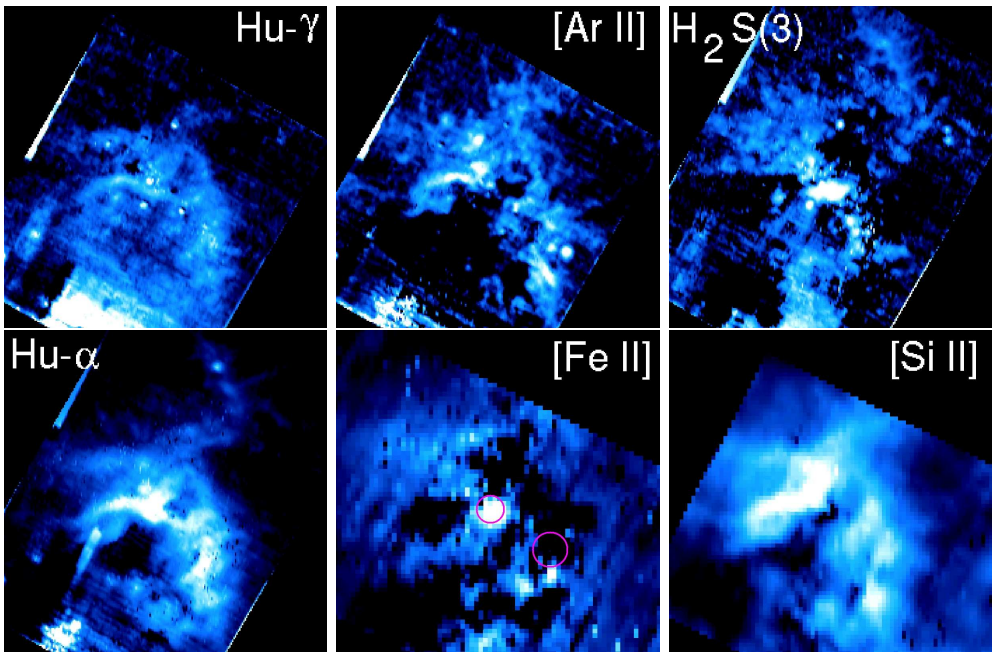

Fig. 12.— The faintest fitted atomic line maps from Figure 10, each reproduced at a scale that brings out detail. In order: Humphreys-γ λ5.90μm, [Ar II]λ7.0μm, H_2 S(3) λ9.67μm, Humphreys-α λ12.37μm, [Fe II]λ26.0μm, [Si II]λ34.8μm. The magenta circles on the [Fe II] map mark the detected peaks of [O I]λ63.1μm and [N III]λ57.3μm.

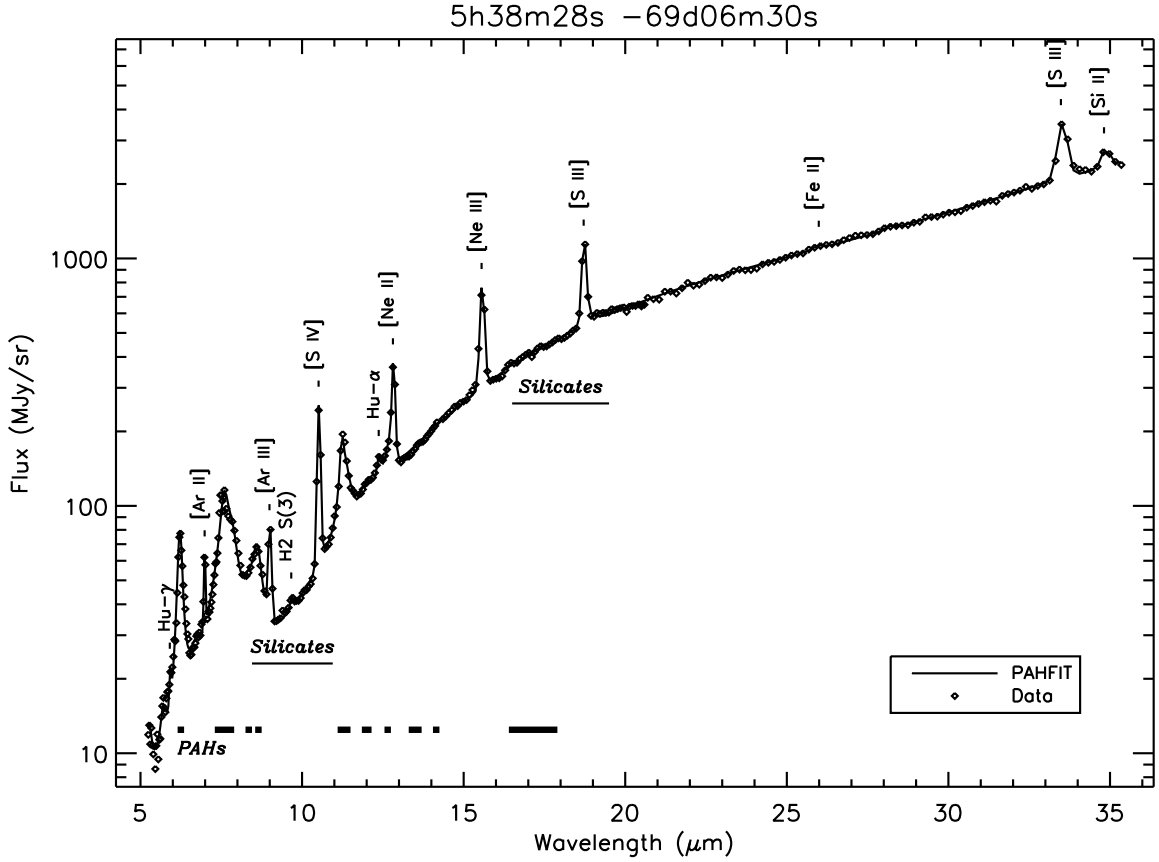

Fig. 13.— The IRS spectrum at $5^h38^m28^s$ -69°06′30″, where there is a peak in Ar and a local minimum of excitation (see source C on Figure 2). The most prominent atomic lines in the 30 Doradus MIR spectrum are labeled, as are the bands of silicate absorption and the major bands of PAH emission.

3.2. Line Ratios

Figure 14 shows the three line ratio maps [Ar III]λ9.0μm/[Ar II]λ7.0μm, [Ne III]λ15.5μm/[Ne II]λ12.8μm, and [S IV]λ10.5μm/[S III]λ33.4μm. These species all have ionization potentials above 13.6eV, and thus are sensitive to the shape or hardness of the ionizing spectrum (we will call this T_{rad}, because it is often parametrized by the best-fitting black-body over λ <912Å) and the intensity of ionizing radiation. The latter is usually quantified as the dimensionless ionization parameter

$$U = \frac{1}{n}\int_{13.6eV}^{\infty} \frac{F_\nu}{ch\nu} d\nu,$$

or ratio of ionizing photon density to atom density. Any single line ratio cannot distinguish between elevated U or T_{rad}, but because the spacing of the ionization potentials differs with atom, different ratios have different U and T_{rad} dependencies, and measuring two ratios can break the degeneracy. (This has been discussed by many authors, see especially the discussions in Morisset et al. 2004; Martín-Hernández et al. 2002; Dopita et al. 2006, ,and §5.1 and Fig 20 below.).

All ratios increase with U, but locations where the ratios are not well correlated can indicate changes in the hardness of the ionizing field. In 30 Doradus the ratios are very well correlated (correlation coefficient of 0.7 between the Ne ratio and Ar ratio map, 0.8 between the Ne and S ratios, and 0.7 between the Ar and S ratios). Figure 17 shows a spatially resolved measure of correlation between the Ne and S ratio maps,

$$\frac{R_S - \langle R_S \rangle}{\langle R_S \rangle} \frac{R_{Ne} - \langle R_{Ne} \rangle}{\langle R_{Ne} \rangle},$$

where R_S =log([S IV]/[S III]), R_{Ne} =log([Ne III]/[Ne II]), and angle brackets indicate averages over the map. This quantity is positive where the two maps are most similarly greater or less than their respective means, and negative where the ratios differ relative to their respective means. The Ne and S ratios are telling us similar things over much of the region, in particular high excitation in a "hot spot" at $5^h38^m42^s$ -69°05′17″ between the two lobes of the ridge and in the region to the south of the bubble, and a low excitation ridge to the north.

One question that is possible to investigate with this dataset is whether embedded star formation in the ridge affects gas excitation measured in the infrared, that otherwise might be concealed by extinction and unrelated diffuse emission at other wavelengths. On Figure 15 we plot the 3.5μm-excess sources of Maercker & Burton (2005), representing a possibly incomplete list of embedded young stars. The protostellar candidates are concentrated along the IR-bright ridge, but do not show any particularly striking correlation with regions of high excitation – in fact the southern part of the region has high excitation and few prototellar candidates.

It is also interesting to note the locations of main-sequence (and post-main-sequence) massive stars in the region, and whether those are associated with regions of elevated excitation. In Figure 16 we show the location of Wolf-Rayet stars and early O stars (there are discrepencies between spectral types determined by different authors, and our intent is to show the most massive stars, not provide

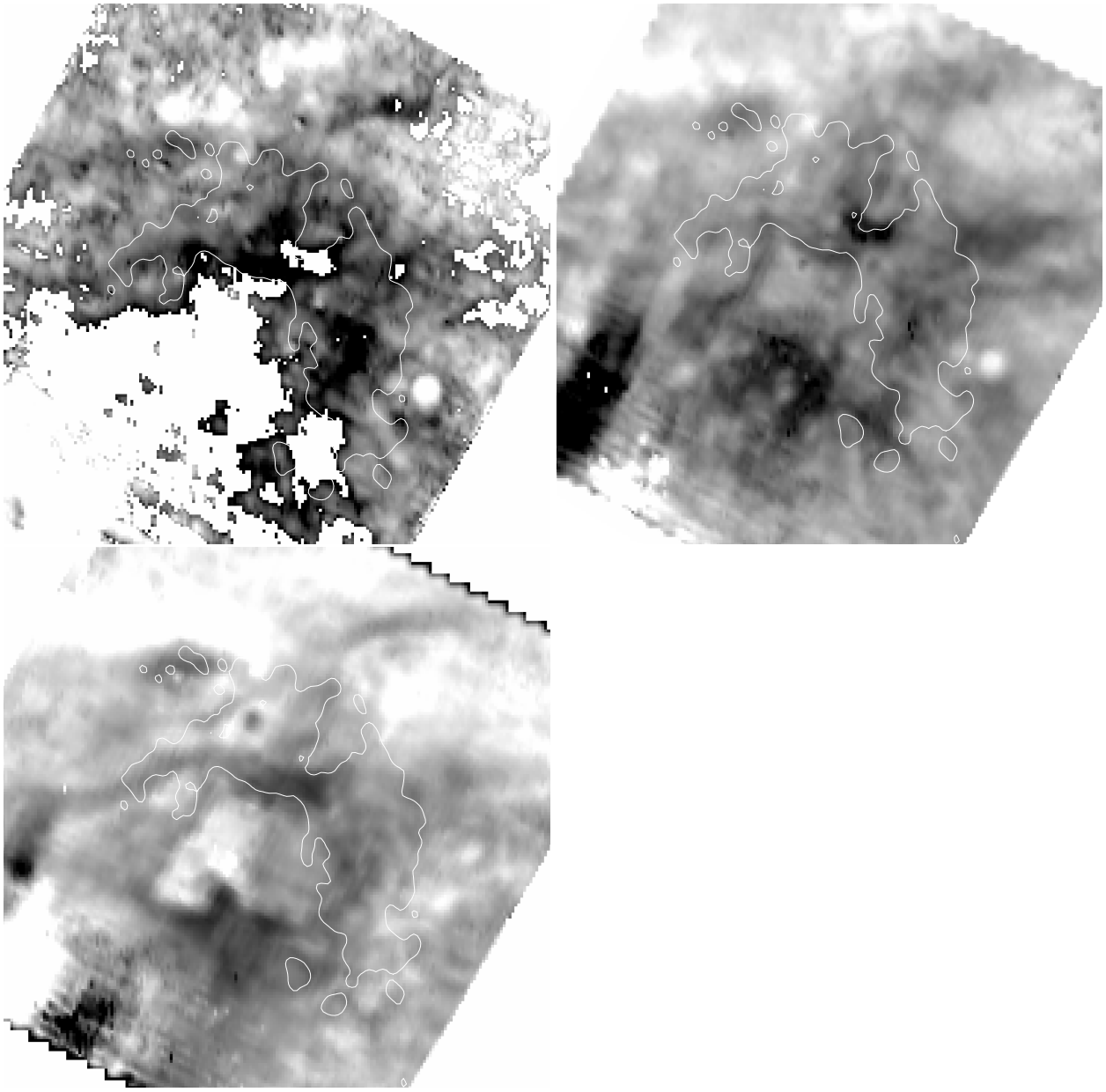

Fig. 14.— Ar, Ne, S Line ratios. A single low contour of 3cm continuum emission is shown to orient the eye and allow easier comparison between maps. Ratio maps and other figures below will cover the same region and display the same 3cm contour.

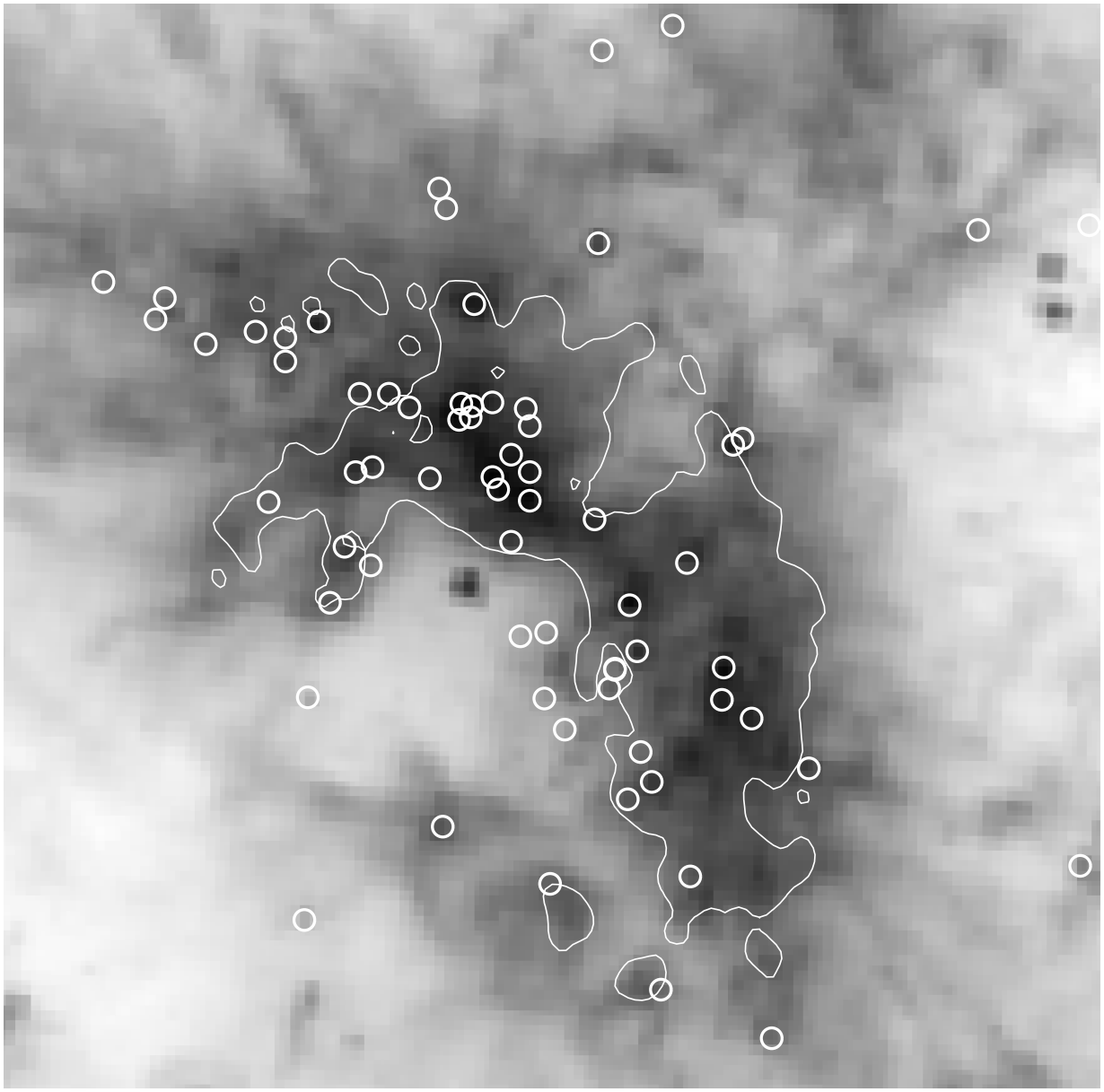

Fig. 15.— Protostellar candidates determined from 3μm excess emission by Maercker & Burton (2005), shown on the SAGE IRAC 8μm image with a single contour of 3cm continuum from Lazendic et al. (2003).

the most precise typing possible). There is a cluster of WR stars between the two lobes of the ridge, coincident with very high excitation gas. There is not a dramatic increase of excitation centered on R136, although the excitation is generally high in the area.

The location noted above for low Ar emission is significantly low in all three line ratios, and in fact three parsec-sized regions of low excitation are prominent on the western side of the region, at $5^h38^m27^s$ -69°06′29″, $5^h38^m30^s$ -69°06′25″, and $5^h38^m24^s$ -69°06′00″. There is little 3cm continuum at those locations, which lie almost exactly on the opposite side of a molecular cloud from R136. The easternmost low-excitation spot is near a 3.5μm-excess protostellar candidate (Maercker & Burton 2005, and Fig. 15), but the other two locations are not. High resolution and sensitivity molecular observations may reveal dense, starless molecular clumps in this part of 30 Doradus, (self)-shielded from the intense radiation.

Interestingly, the Ne and S line ratios show quite different behaviour on the eastern edge of the bubble, where [Ne III]/[Ne II] is high but [S IV]/[S III] is low. The S ratio is more affected by extinction since [S IV]λ10.5μm is in the silicate dust absorption feature, so that could be a region of high extinction [quantify how much extinction is required], or a region of particularly hard ionizing radiation.

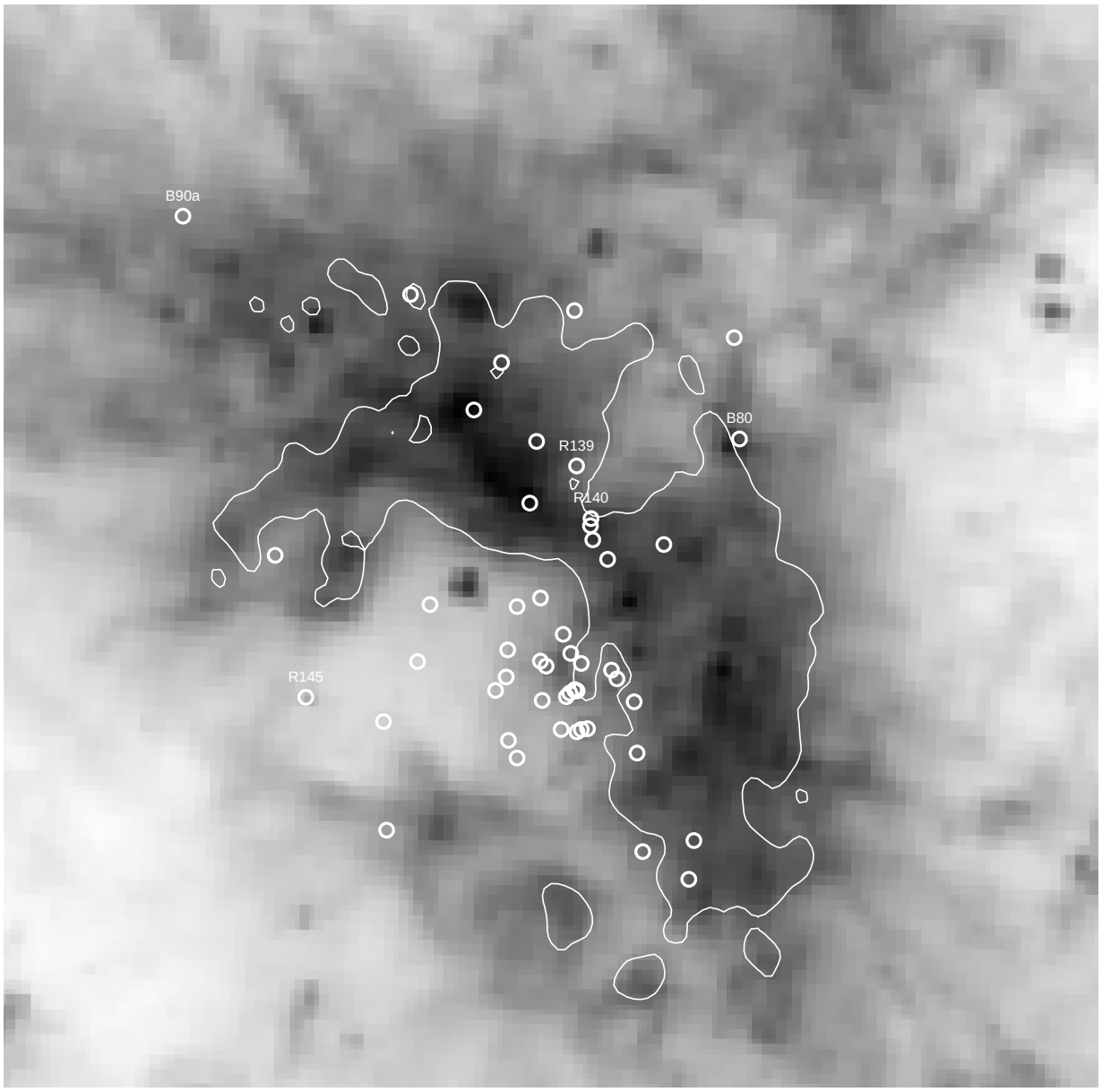

Fig. 16.— The most energetic stars in the region - Wolf-Rayet stars and early O stars, from Breysacher et al. (1999); Parker (1993).

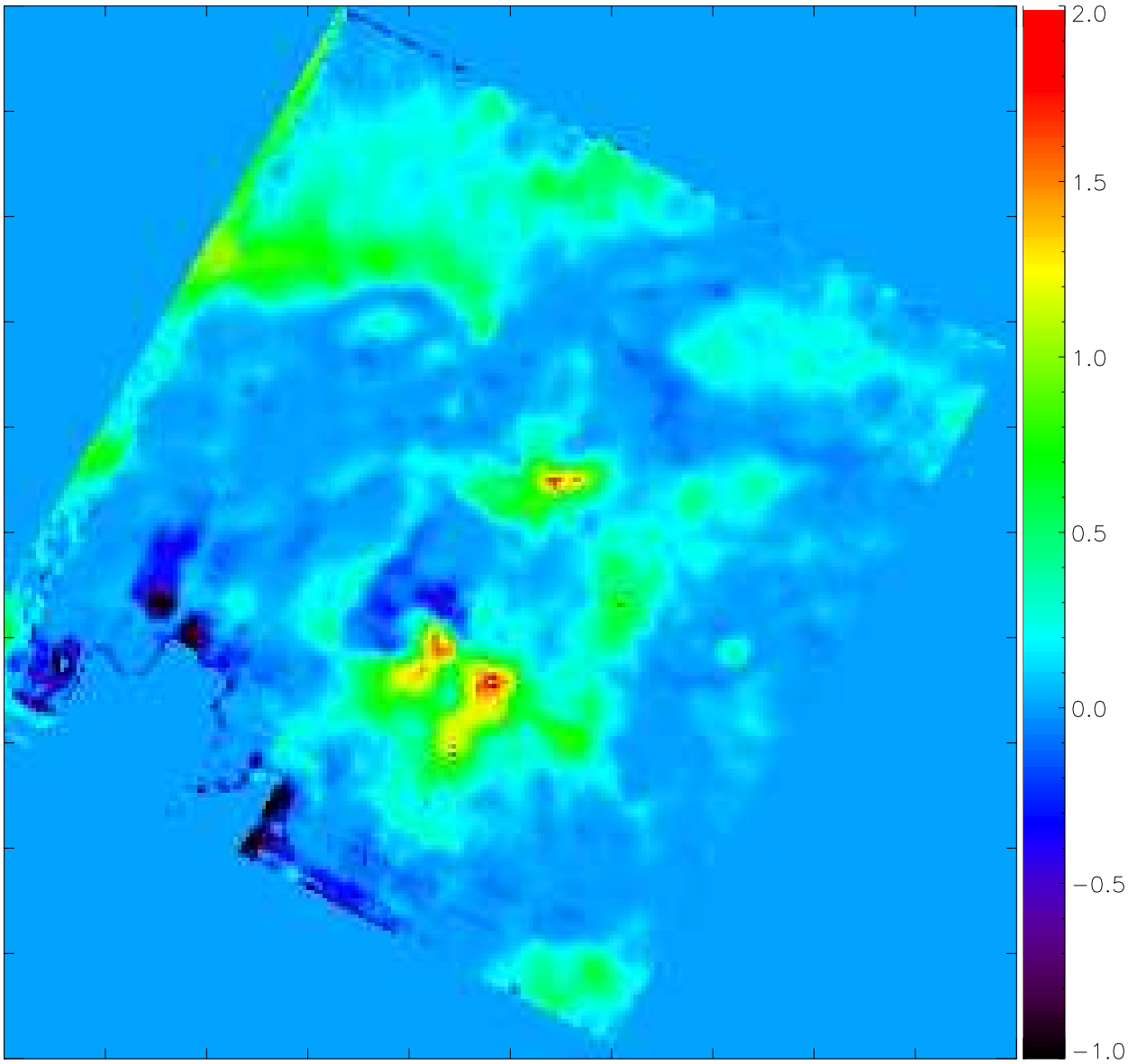

Fig. 17.— Map of how well correlated [Ne III]/[Ne II] is with [S IV]/[S III]- this image is positive where the ratios are similarly large or small, and negative where they differ. As discussed in the text, the former most likely indicate changes in U, and the latter may indicate changes in the hardness of the ionizing field.

4. Distribution of Matter: Extinction and n_e

4.1. Extinction

Previous estimates of the extinction in 30 Doradus found A_V=1.1±0.1mag (Dickel et al. 1994, and refs therein), with two possible locations of higher extinction at $05^h38^m39^s$ -69°07′30″ and $05^h38^m32^s$ -69°06′22″. Rosa & Mathis (1987) found extinction corrections at Hβ of 0.5-1.0 (A_V=0.4-0.8) at ten locations in the outer parts of the region we are studying. We make three estimates of extinction in the region, two directly from our dataset. All methods suffer from systematic uncertainty and modest signal-to-noise, but we can be confident of higher extinction in the regions that all three methods agree.

First we follow the procedure used in Lazendic et al. (2003), with their centimeter data that they kindly provided, to derive a map of extinction in 30 Doradus (blue, in Fig. 18). We assume that all of the centimeter continuum emission in the 30 Doradus region is thermal. Single dish measurements estimated that the broad nonthermal component contributes less than 2% at 6cm (Shaver et al. 1983, and refs therein). Lazendic et al. (2003) identified two possible supernova remnants from comparison of cm synthesis images and optical recombination lines, but their own analysis and subsequent followup with optical and Xray imaging and optical spectroscopy suggests that these are merely extinguished H II regions (Chu et al. 2004). The relationship between thermal brehmstrahlung centimeter continuum and hydrogen recomination line emission depends weakly on the electron temperature, but Rosa & Mathis (1987) and Peck et al. (1997) both found that T_e variations are small in 30 Doradus ($\lesssim$ ±300K), so it unlikely that the calculated extinction variations are actually misinterpreted T_e variations.

We derived two more maps of extinction directly from the IRS spectral cube. Amorphous silicate dust is responsible for two broad bands of absorption at 9.7 and 18 μm (Chiar & Tielens 2006). The PAHFIT package reports the fitted optical depth at 9.7 μm. The resulting map for 30 Doradus is shown in Figure 18, in green. The fit to the absorption feature is sensitive to noise in the spectrum. We cropped away southern parts of the map that were clearly artifacts, and any part of the map where the signal-to-noise was less than 2. Finally, we median-smoothed the resulting map with a window of 3 pixels. The result is a sparse map showing the regions of comparatively reliable elevated silicate absorption.

The ratio of Hydrogen recombination line strengths can also be used to calculate extinction, most commonly by assuming an intrinsic (unextincted) ratio from Case B recombination. Our dataset includes Humphreys-α (7-6) and Humphreys-γ (9-6), Due to modest signal-to-noise and to an unidentified feature that forms a low-level broad plateau in the region of the Humphreys-α λ12.37μm line (sometimes causing the continuum to be underestimated in our fits), the absolute value of extinction calculated from this ratio has a large systematic uncertainty. Further systematic uncertainty arises in the choice of extinction curve, since the lines lie on the wings of the silicate absorption features, which vary in amplitude and width in different studies. However, all extinc-

tion curves that we considered show greater relative extinction at Humphreys-α λ12.37μm than at Humphreys-γ λ5.90μm. We examined the extinction curves of Chiar & Tielens (2006) for the Galactic Center and the ISM, and the average LMC extinction curve[3] based on the carbonaceous-silicate grain model of Weingartner & Draine (2001). All of the extinction curves roughly agree in the vicinity of the Humphreys-α emission line. Near the Humphreys-γ line, the Chiar & Tielens curves agree well with the near-infrared extinction for the ISM found by Indebetouw (Chiar & Tielens 2006). Thus, extinction correlates with the flux ratio of Humphreys-γ λ5.90μm to Humphreys-α λ12.37μm, and we can still find the relative level of extinction across 30 Doradus from the Humphreys-α/ Humphreys-γ ratio, even though the absolute normalization is uncertain.

We calculated the signal-to-noise of the ratio based on the RMS variance of the individual maps of emission line strength, and removed all regions of the map where the signal-to-noise was less than 2. We cropped away the parts of the map where an additive correction was made to the SL spectra (see §2.1.4), because this subset of the map encloses some spectra which have a unphysical plunge at the red edge of the SL2 module. The fit to those spectra generally underestimates the continuum near the Humphreys-γ line, and thus overestimates the ratio of Humphreys-γ to Humphreys-α. Finally, we also cropped away the parts of the map where the reduced χ^2 of the fit was greater than 5. The ratio map shown in red in Figure 18 is now mainly limited to those areas of 30 Doradus where we obtained both good detections of these two faint lines and a good fit, though some of the brighter areas at the edges of the ratio map are probably still unreliable.

The areas where all three methods agree on especially high extinction have been marked on Figure 18. As we shall discuss below, extinction has a small effect on the Neon excitation ratio, but raises the [S IV]/[S III] (due to the shape of the extinction curve), which in turn will get interpreted as higher T_{rad} in our photoionization models. The regions of interestingly high T_{rad} do not turn out to correspond to regions of clearly high extinction, but the effect should be kept in mind in interpreting the data.

4.2. Electron Density

Figure 19 shows the electron density calculated from [S III]λ18.7μm/[S III]λ33.4μm. The [S III]λ18.7μm map was convolved to the lower resolution of the [S III]λ33.4μm map, and the line ratio converted to electron density using the conversion in Dudik et al. (2007) at T_e=10^4K. The ridge is prominent, and in fact the n_e map is quite similar to the 3cm continuum in morphology. The density is elevated to the south of the bubble and R136, in a region of relatively high excitation.

[3]Available at: www.astro.princeton.edu/~draine/dust/dustmix.html

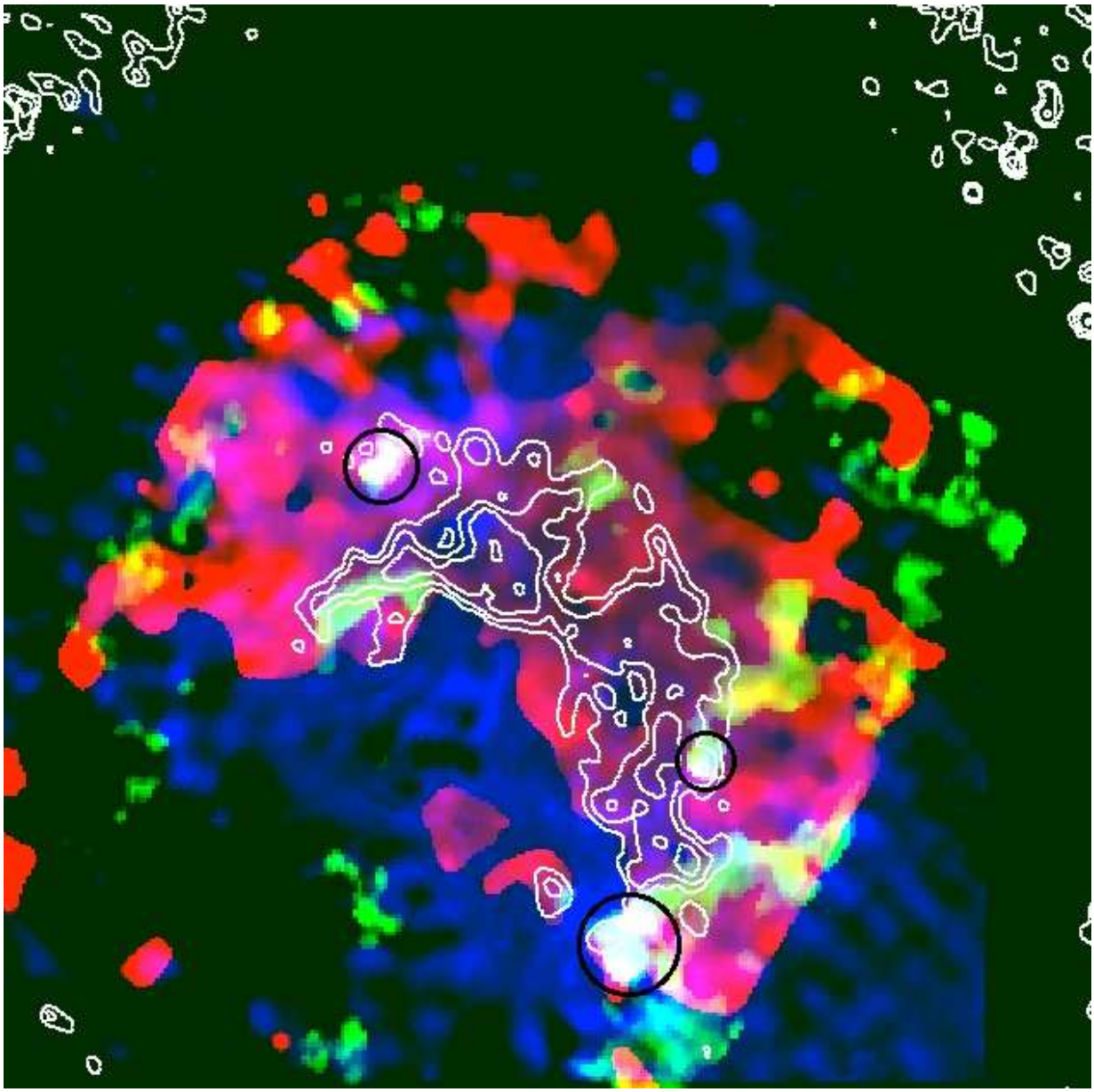

Fig. 18.— Three-color map of extinction in 30 Doradus. Red: the IRS Humphreys-γ/ Humphreys-α ratio, which is proportional to extinction. Green: the optical depth of silicate absorption from the IRS spectral map. Blue: Extinction calculated from the ratio of 3cm continuum (Lazendic et al. 2003) to Hα emission ()[ref needed]. White contours show the high-resolution 3cm continuum. The red and green maps have been cropped to remove artifacts or regions of low signal-to-noise (see text). Some of the bright areas near the edges of the red map may still be artificial and should be regarded with caution. The areas where all three maps agree on especially high extinction have been marked in black. The northeasternmost corresponds with source B marked on Figure 2.

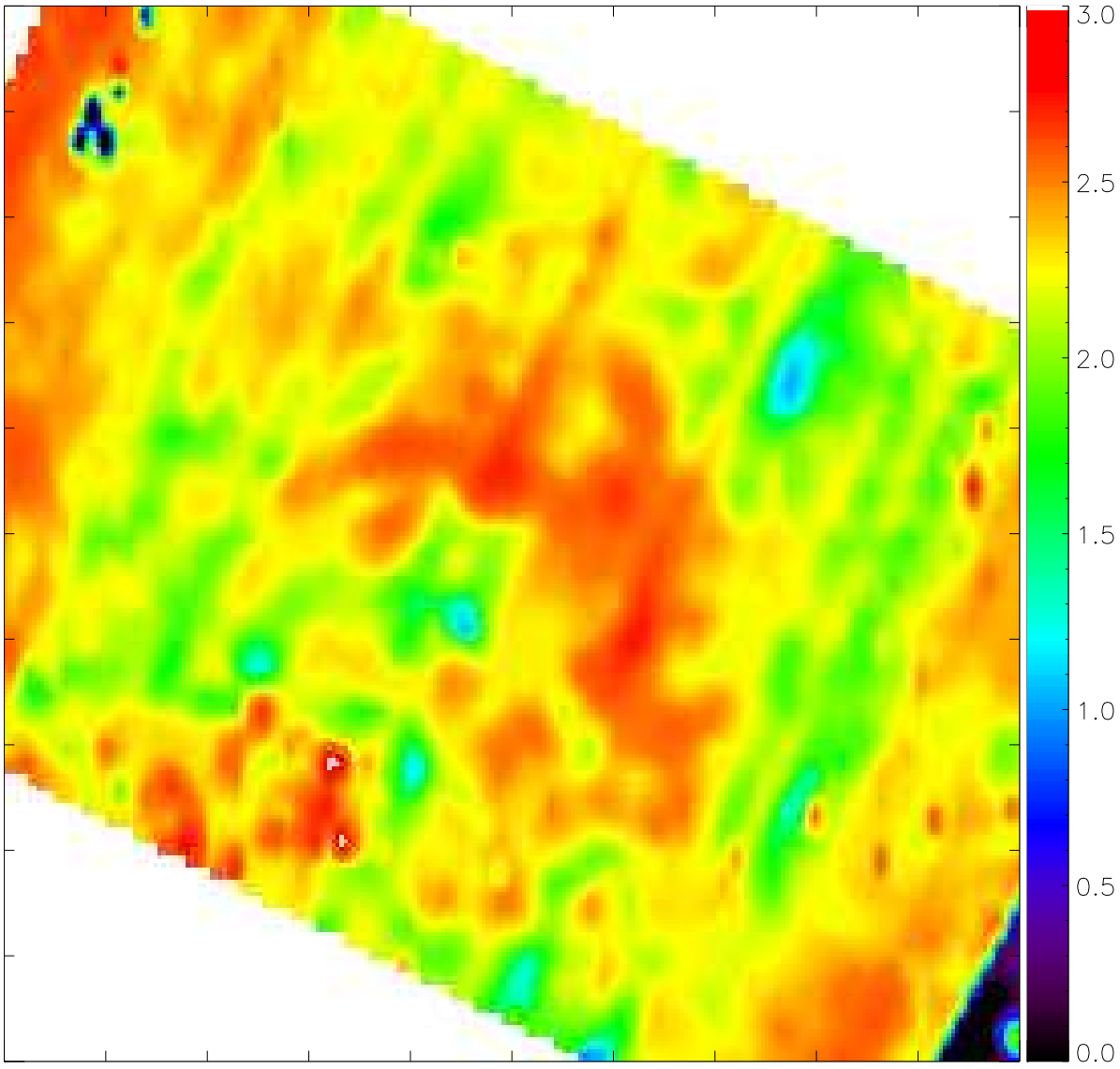

Fig. 19.— n_e calculated from [S III]λ18.7μm/[S III]λ33.4μm. The ridge is prominent, as well as a region of increased density to the south.

4.3. Abundances

Peck et al. (1997) found no significant variations on 15″ scales in the He abundance $Y^+ = He^+/H^+ = 0.13\pm0.02$ measured from radio recombination lines. Their mean value is slightly higher than the value of 0.08±0.01 found by Rosa & Mathis (1987) from optical emission lines. The latter authors found Ne/O, S/O, and Ar/O ratios close to solar, but an O/H ratio 1/3 solar ($2.12\pm0.31\times10^{-4}$). Small scale abundance variations in H II regions including 30 Doradus (Tsamis & Péquignot 2005) have been proposed to explain discrepencies between optical and infrared abundance determinations. We might hope to detect sub-parsec scale abundance variations in this dataset by using three infrared line ratios to solve simultaneously for U, T_{rad}, and Z. In practice, we find that the excitation variations can be adequately explained without abundance variations, which would be seen as residuals in our fitting of U and T_{rad}. The signal-to-noise especially in our Argon line ratio is insufficient to detect abundance *variations* at the 0.1 dex level predicted by Tsamis & Péquignot (2005). We do find that on average, relatively high abundances (still sub-solar, but greater than 0.1 solar) result in better agreement between the three infrared line ratios in our photoionization models, although systematic effects such as the Argon recombination rate have a larger effect on this agreement than the abundances (Morisset et al. 2004; Stasińska & Schaerer 1997).

[add a nod here to Lebouteiller and Brandl highres paper?]

5. Distribution of Radiation and Gas: Excitation

5.1. Photionization models

As mentioned above, if photoionization is assumed to be the dominant physical process, the ionic line ratios depend on U, T_{rad}, and to a lesser degree metallicity. If one assumes constant abundances and hardness or T_{rad}, then the line ratio maps in Figure 14 are maps of the ionization parameter U, varying from log $U \simeq$-3 to log $U \simeq$-1.5.

A somewhat more sophisticated analysis is to solve for T_{rad} and U simultaneously. We prepared a grid of photoionization models using Cloudy (Ferland et al. 1998) as a 0-dimensional tool to solve for the ionization structure and line emissivities given a specified radiation field and ionization parameter (we used the output of the first zone in each simulation). We explored different input spectra, including ATLAS (Castelli & Kurucz 2004) and Costar OB and Wolf-Rayet atmospheres (Schaerer & de Koter 1997; Smith et al. 2002), and black-bodies. We also varied the dust prescription in terms of abundance and grain size. Neither had a strong effect on the line ratios as a function of T_{rad} and U, provided that U was calculated locally, i.e. from integrating the diffuse ionizing field in the simulation above 1 Ry, rather than assuming some geometry-dependent expression such as $N_\star/c4\pi r^2 n_e$.

Figure 20 shows typical behaviour - each measured ratio defines a curve in $U - T_{rad}$ space,

but the lines have different slopes because the ionization potentials are spaced differently for the different atoms. This is equivalent to the parallel arrows for U and T_{rad} in Morisset et al. (2004) (see also Martín-Hernández et al. 2002; Dopita et al. 2006). Two measured ratios can better constrain U and T_{rad}. We will focus on the Ne and S ratios since [Ar II] is not detected over large parts of the H II region, but the Ar ratio will be used in discussion where it constrains the interpretation.

Figure 21 shows the fitted U and T_{rad} across 30 Doradus. The ridge is a region of high ionization parameter, as previously noted from simple examination of the line ratios. The region around the relatively isolated source at $5^h38^m56.5^s$ -69°04′17″ to the north of the ridge is also highly excited, probably due to the local effects of that star (source "B", Figure 2). We note two regions of high U in particular. The most prominent is between the two parts of the ridge, where young stars may be locally ionizing the gas and beginning to lower the density and disperse the ridge (see Figure 15 for the location of protostars, and Figure 16 for the locations of the most energetic optically identified stars). Alternately, the density is simply lower there and ionizing radiation can more easily leak out from the bubble region around R136. The northern side of this "hot spot" shows evidence for hardening of the radiation field, which could result of the radiation originates in the bubble or on its rim, and is propagating northward, and being absorbed by gas and dust (both of which will harden the field). The high degree of porosity and mixing between molecular and ionized material in 30 Doradus is well known (see e.g. Poglitsch et al. 1995). On the south side of the bubble is another region of high ionzation parameter - this region also shows high electron density in the [S III] ratio, so the field must be locally strengthened, perhaps by the WR stars known in that region (Fig 16). Particulary interesting is the region on the eastern side of the bubble, which shows up in the fitted parameter maps as high T_{rad}, but not particularly high U. There is a single catalogued Wolf-Rayet star (R145, WN6 type) in the center of that area, which may be energizing the eastern end of the bubble.

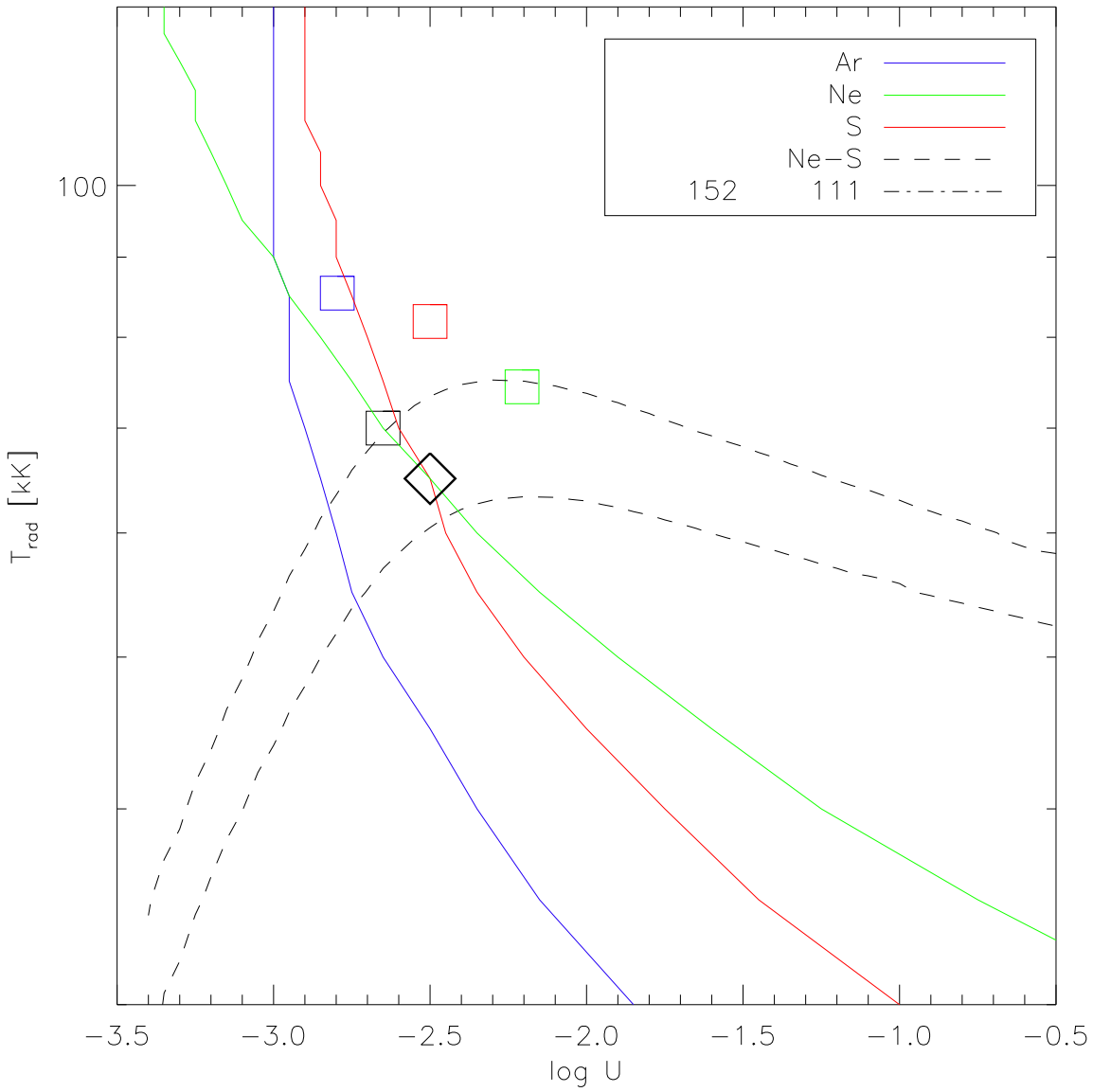

Fig. 20.— Fits to U and T_{rad} at a representative location $05^h38^m37^s$ -69°06′12″. Loci of consistency with the data are shown for fitting Ar, Ne, and S ratios alone (lines from upper left to lower right), the difference between the S and Ne ratios (log([S IV]/[S III])-log([Ne III]/[Ne II]), dashed lines, 1-sigma confidence interval shown), and the combination of all ratios (bold diamond). See text for discussion. [add arrows for what extinction does]

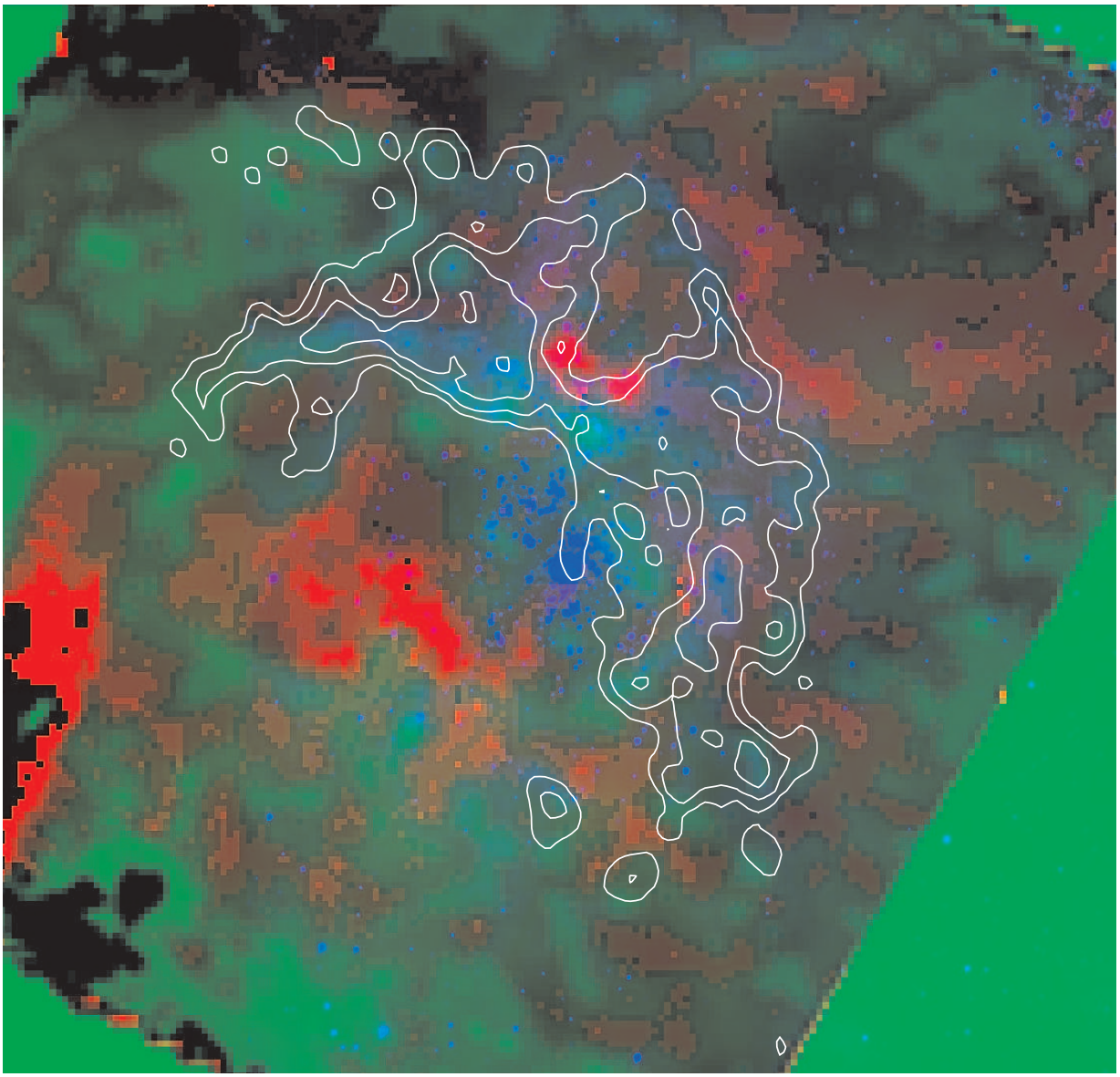

Fig. 21.— Fitted T_{rad} (red) and U (green) based on the S and Ne line ratios. Optical V band in blue shows the location of stars and R136 in particular, and white contours show the high-resolution 3cm continuum from Lazendic et al. (2003).

5.2. Shock Models

Protostellar shocks can also produce MIR fine-structure emission, but only if the excitation (shock velocity) is high enough. [Ne II] requires J-shocks with v$\gtrsim$60km s^{-1} Hollenbach & McKee (1989) and [Ne III] velocities in excess of 100km s^{-1} Molinari & Noriega-Crespo (2002). Lefloch et al. (2003) detect [Ne II]λ12.8μm and [Ne III]λ15.5μm in HH 2, but only from the highest excitation working surface. Similar results are being found with *Spitzer*, detecting [Ne II]λ12.8μm but not [Ne III]λ15.5μm, and [S III]λ33.4μm but not [S IV]λ10.5μm in HH46/47 (Noriega-Crespo et al. 2004), Cep E (Noriega-Crespo et al. 2004), and HH7-11 and 54 (Neufeld et al. 2006). Even the bow shock near a runaway O9.5 star (France et al. 2007) and the stronger shocks in SNR (Neufeld et al. 2007) show similarly relatively low-excitation MIR emission.

The (few) MIR observations of regions containing both shocks and photoionization tend to show photoionization dominant. In [Ne II] and [S IV] maps of the massive star formation region W51 IRS2, high spectral resolution mapping with TEXES (Lacy et al. 2007) allows the high velocity emission to be separated from that at the velocity of the molecular cloud. The authors do not note dramatically different line ratios in the high velocity emission from that at the systemic velocity, but rather confirm earlier ground-based observations of MIR fine structure lines consistent with photoionization by late O-type stars (Okamoto et al. 2001). Lacy et al. (2007) interpret their observations as a neutral jet emerging from the molecular cloud and being subsequently photoionized.

More recent work with *Spitzer* in the Galactic center (Simpson et al. 2007) cannot produce the observed O^{+3} with any reasonable photoionziation model, even including hot supergiant atmospheres and 10^{5--6}K blackbodies representing diffuse X-ray emission. The proposed alternative of $\sim$100km s^{-1} shocks can match the observed O IV. The authors do not *require* shock excitation to explain their Ne and S line ratios, but do note that the highest excitation gas is found between the two stellar clusters, which is indicative of shock excitation.

We ran a set of shock models using John Raymond's code (Raymond 1979; Cox & Raymond 1985; Hartigan et al. 1987) with a range of velocities and pre-shock densities. The ratios of relevant fine-structure lines are shown in Figure 22, along with the observed ranges in 30 Doradus. To first order, all three ratios can be matched with shocks on the order of a few hundred km s^{-1} in quite low-density gas ($n < 1$cm^{-3}). However, we have significant nondetections of the higher ionization species [O IV] and [Ne V], with 3-σ upper limits less than 10^{-2} relative to [S III]λ18.7μm across the map. The predicted ratios for those two species relative to [S III] are also calculated, and while [Ne V] is marginally consistent, shocks of this order should produce easily detectable [O IV]. Thus we conclude that in 30 Doradus as elsewhere, although shocks certainly exist, the ionization structure of the gas is dominated by photoionization and not shock activity.

It is particularly interesting to consider the "hot" region on the eastern side of the bubble where the photoionization models are driven to high T_{eff} and moderate U by low [S IV]/[S III] and moderate [Ne III]/[Ne II]. That low [S IV]/[S III] ratio makes this part of 30 Doradus more

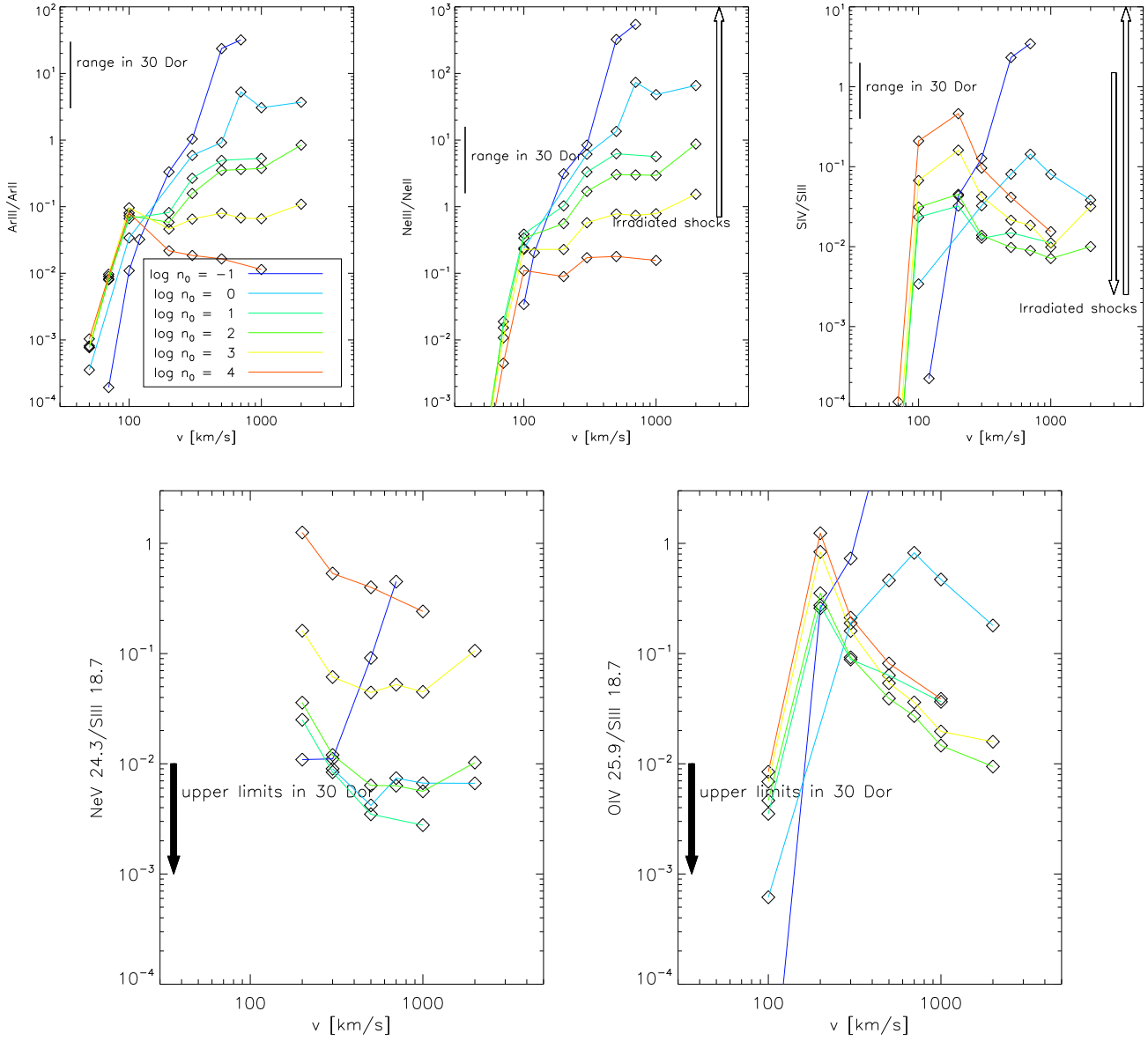

Fig. 22.— Ion ratios calculated from plane-parallel shock models. Although the Ne, Ar, and S ratios can be produced by shocks of a few 100km s^{-1} in diffuse gas, those shocks should also produce [O IV] emission, which we do not detect on 30 Doradus.

consistent with shock models than other parts, although the nondetections of [O IV] and [Ne V] are still problematic. We suggest that of anywhere in the nebula, the eastern end of the bubble may have the highest likelihood of excitation by shocks, as would be expected from winds of the WN6 star located there hitting the denser sides of an evacuated bubble.

6. Conclusions

We present an infrared data cube of 30 Doradus, observed with the InfaRed Spectrograph on the *Spitzer* Space Telescope. Aromatic dust emission features are of moderate strength in the 30 Doradus region, increasing in strength with increasing distance from the central R136 cluster. Detailed analysis of the dust content of the region from these features will follow in a subsequent publication. Of the pure rotational lines of molecular hydrogen, only S(3)λ9.67μm is detected with any significance, peaking on the bright "ridge" that dominates the morphology of the region at many wavelengths. Low-ionization atomic lines are present but not particularly strong: [Si II] is detected in the outskirts of the mapped region, outside the region of strongest centimeter continuum (highest emission measure ionized gas). [Fe II] λ26.0μm is only tenatively detected in two locations.

Two hydrogen recombination lines Huα (7-6) and Huγ (9-6) can be mapped over a large fraction of the observed area, and from these a relative measure of the extinction can be calculated. Independent estimates of the extinction are calculated from fitting the strength of the 10μm silicate feature, and from the ratio of Hα to centimeter continuum. While none of the three extinction measures is extremely high signal-to-noise, the locations where all three show higher extinction should be quite secure - in particular three distinct locations in the west, southwest, and northeast, outside of the "ridge" (Fig 18).

The strongest features in the data cube are the moderate-ionization ionic lines [Ar II]λ7.0μm, [Ar III]λ9.0μm, [Ne II]λ12.8μm, [Ne III]λ15.5μm, [S III]λ18.7μm, [S III]λ33.4μm, and [S IV]λ10.5μm. These lines are most sensitive to physical conditions in the ionized gas: the ionization parameter U and hardness of the ionizing field, parametrized by the radiation temperature T_{rad}. We fit the Neon and Sulphur ratios with photoionization models to derive a 2-dimensional map of U and T_{rad}. We find that the excitation generally follows the "ridge and bubble" morphology,and that under the assumptions of pure photoionization, there are "hot spots" of hardened ionizing field in the east of the bubble and between the two lobes of the ridge (corresponding to two molecular clouds). We also compare the line ratios to shock models and find poorer agreement with the data. In particular the nondetections of more highly ionized species O IV and Ne V suggest that photoionization dominates over collisional excitation by shocks. Overall, the local effects of hot stars in 30 Doradus (such as the single WR star on the eastern side of the bubble) appear to dominate over any large-scale trend with distance from the central cluster R136.

ACKNOWLEDGMENTS

This work benefitted greatly from the generous contributions of several individuals: Gary Ferland and his students for creating the Cloudy photoionization code, John Raymond for giving us a copy of his shock code, John Dickel and Jasmina Lazendic for giving us their calibrated centimeter snythesis images, and Sean Points for giving us calibrated MCELS Hα data. This publication would not have been possible without extensive use of NASA's Astrophysics Data System Bibliographic Services, and the SIMBAD database, operated at CDS, Strasbourg, France. This publication makes use of data products from the Two Micron All Sky Survey, which is a joint project of the University of Massachusetts and the Infrared Processing and Analysis Center/California Institute of Technology, funded by NASA and NSF. Data from the *Spitzer* Space Telescope (operated by the Jet Propulsion Lab for NASA) are taken from PID 30653 "Stellar Feedback on Circumcluster Gas and Dust in 30 Doradus, the Nearest Super-Star Cluster" and PID 20203 "Spitzer Survey of the Large Magellanic Cloud: Surveying the Agents of a Galaxy's Evolution (SAGE)" GdM and RI were supported in part by Spitzer/NASA/JPL grant [find 30dor grant number], and RI in part by a Spitzer fellowship to UVa.

Facilities: Spitzer (IRS)

REFERENCES

Bernard, J.P. 2008, AJ submitted.

Bochsler, P. 2007, A&A, 471, 315

Brandl, B.R. 2005, preprint(astro-ph/0501572)

Breysacher, J., Azzopardi, M., & Testor, G. 1999, A&AS, 137, 117

Castelli, F., & Kurucz, R. L. 2004, ArXiv Astrophysics e-prints, arXiv:astro-ph/0405087

Chiar, J. E., & Tielens, A. G. G. M. 2006, ApJ, 637, 774

Chu, Y.-H., Gruendl, R. A., Chen, C.-H. R., Lazendic, J. S., & Dickel, J. R. 2004, ApJ, 615, 727

Cox, D. P., & Raymond, J. C. 1985, ApJ, 298, 651

Dickel, J. R., Milne, D. K., Kennicutt, R. C., Chu, Y.-H., & Schommer, R. A. 1994, AJ, 107, 1067

Dopita, M. A., et al. 2006, ApJ, 639, 788

Dudik, R. P., Weingartner, J. C., Satyapal, S., Fischer, J., Dudley, C. C., & O'Halloran, B. 2007, ApJ, 664, 71

Fazio, G. G., et al. 2004, ApJS, 154, 10

Ferland, G. J., Korista, K. T., Verner, D. A., Ferguson, J. W., Kingdon, J. B., & Verner, E. M. 1998, PASP, 110, 761

France, K., McCandliss, S. R., & Lupu, R. E. 2007, ApJ, 655, 920

Giveon, U., Sternberg, A., Lutz, D., Feuchtgruber, H., & Pauldrach, A. W. A. 2002, ApJ, 566, 880

Hartigan, P., Raymond, J., & Hartmann, L. 1987, ApJ, 316, 323

Hollenbach, D., & McKee, C. F. 1989, ApJ, 342, 306

Houck, J. R., et al. 2004, Proc. SPIE, 5487, 62

Hunter, D.A. 1999, IAUS, 190, 217

Hyland, A. R., Straw, S., Jones, T. J., & Gatley, I. 1992, MNRAS, 257, 391

Johansson, L. E. B., et al. 1998, A&A, 331, 857

Johnson, K. E. 2004, New A Rev., 48, 1337

Kim, S. 2007, The Seventh Pacific Rim Conference on Stellar Astrophysics, 362, 297

Kothes, R., & Dougherty, S. M. 2007, A&A, 468, 993

Krabbe, A. C., & Copetti, M. V. F. 2002, A&A, 387, 295

Lacy, J. H., et al. 2007, ApJ, 658, L45

Lazendic, J. S., Dickel, J. R., & Jones, P. A. 2003, ApJ, 596, 287

LeBouteiller [sp?], V. et al. 2008 in preparation.

Lefloch, B., Cernicharo, J., Cabrit, S., Noriega-Crespo, A., Moro-Martín, A., & Cesarsky, D. 2003, ApJ, 590, L41

Maercker, M., & Burton, M. G. 2005, A&A, 438, 663

Madden, S. C., Galliano, F., Jones, A. P., & Sauvage, M. 2006, A&A, 446, 877

Martín-Hernández, N. L., et al. 2002, A&A, 381, 606

Meixner, M., et al. 2006, AJ, 132, 2268

Morisset, C., Schaerer, D., Bouret, J.-C., & Martins, F. 2004, A&A, 415, 577

Molinari, S., & Noriega-Crespo, A. 2002, AJ, 123, 2010

Neufeld, D. A., et al. 2006, ApJ, 649, 816

Neufeld, D. A., Hollenbach, D. J., Kaufman, M. J., Snell, R. L., Melnick, G. J., Bergin, E. A., & Sonnentrucker, P. 2007, ApJ, 664, 890

Noriega-Crespo, A., et al. 2004, ApJS, 154, 352

Noriega-Crespo, A., Moro-Martin, A., Carey, S., Morris, P. W., Padgett, D. L., Latter, W. B., & Muzerolle, J. 2004, ApJS, 154, 402

Okamoto, Y. K., Kataza, H., Yamashita, T., Miyata, T., & Onaka, T. 2001, ApJ, 553, 254

Parker, J. W. 1993, AJ, 106, 560

Peck, A. B., Goss, W. M., Dickel, H. R., Roelfsema, P. R., Kesteven, M. J., Dickel, J. R., Milne, D. K., & Points, S. D. 1997, ApJ, 486, 329

Peimbert, A. 2003, ApJ, 584, 735

Poglitsch, A., Krabbe, A., Madden, S. C., Nikola, T., Geis, N., Johansson, L. E. B., Stacey, G. J., & Sternberg, A. 1995, ApJ, 454, 293

Raymond, J. C. 1979, ApJS, 39, 1

Rieke, G. H., et al. 2004, ApJS, 154, 25

Rubio, M., Barbá, R. H., Walborn, N. R., Probst, R. G., García, J., & Roth, M. R. 1998, AJ, 116, 1708

Rosa, M., & Mathis, J. S. 1987, ApJ, 317, 163

Shaver, P. A., McGee, R. X., Newton, L. M., Danks, A. C., & Pottasch, S. R. 1983, MNRAS, 204, 53

Schaerer, D., & de Koter, A. 1997, A&A, 322, 598

Sheth, K. 2006, in Spitzer Data Analysis Workshop #4.

Simpson, J. P., Colgan, S. W. J., Cotera, A. S., Erickson, E. F., Hollenbach, D. J., Kaufman, M. J., & Rubin, R. H. 2007, ArXiv e-prints, 708, arXiv:0708.2103

Smith, J.D.T., et al. 2007, ApJ, 656, 770

Smith, J.D.T., et al. 2007, preprint(astro-ph/07083745)

Smith, L. J., Norris, R. P. F., & Crowther, P. A. 2002, MNRAS, 337, 1309

Spitzer Science Center. 2006, Spitzer Space Telescope Observer's Manual, Version 7.1, Spitzer Science Center

Stasińska, G., & Schaerer, D. 1997, A&A, 322, 615

Sturm, E., Lutz, D., Tran, D., Feuchtgruber, H., Genzel, R., Kunze, D., Moorwood, A. F. M., & Thornley, M. D. 2000, A&A, 358, 481

Tsamis, Y. G., & Péquignot, D. 2005, MNRAS, 364, 687

Tsamis, Y. G., Barlow, M. J., Liu, X.-W., Danziger, I. J., & Storey, P. J. 2003, MNRAS, 338, 687

Vermeij, R., & van der Hulst, J. M. 2002, A&A, 391, 1081

Walborn, N.R. 1991, IAUS, 148, 145

Weingartner, J. C., & Draine, B. T. 2001, ApJ, 548, 296.

Werner, M. W., et al. 2004, ApJS, 154, 1